Research Square

Preprints are preliminary reports that have not undergone peer review.
They should not be considered conclusive, used to inform clinical practice,
or referenced by the media as validated information.

Nonlinear dynamic response and mass identification of suspended microchannel resonators

Jie Wang
Institute of Mechanics
Yin Zhang
zhangyin@lnm.imech.ac.cn

Institute of Mechanics

Research Article

Keywords: Resonator, Nonlinear dynamics, Inverse problem, Primary resonance, Method of multiple scales, Mass detection

Posted Date: June 18th, 2026

DOI: https://doi.org/10.21203/rs.3.rs-9884183/v1

License: This work is licensed under a Creative Commons Attribution 4.0 International License.
Read Full License

Additional Declarations: No competing interests reported.

Nonlinear dynamic response and mass identification of suspended microchannel resonators

Jie Wang [1, 2], Yin Zhang [1, 2, *]

[1] State Key Laboratory of Nonlinear Mechanics (LNM), Institute of Mechanics, Chinese Academy of Sciences, Beijing 100190, China

[2] School of Engineering Science, University of Chinese Academy of Sciences, Beijing 100049, China

[*]E-mail address: zhangyin@lnm.imech.ac.cn (Y. Zhang).

Abstract The previous studies on mass detection by using suspended microchannel resonators are mostly based on linear resonance frequency shifts, but the effects of electrostatic actuation forces and nonlinearities are typically neglected. To address this limitation, the model incorporating both electrostatic nonlinearity and beam geometric nonlinearity is developed in this study. The governing equations are derived from Hamilton's principle, and the approximate analytical solutions for the nonlinear amplitude-frequency response are obtained by the perturbation method. Our results indicate that the evolution of the resonance frequencies and the nonlinear amplitude-frequency responses results from the competition between the hardening and softening effects of the geometric and electrostatic nonlinearities. Furthermore, a novel method based on the nonlinear frequency shifts for multi-particle mass detection is proposed. The detection of single and double particles of different masses by using the proposed method is demonstrated by the numerical examples. The robustness of the method under noise influence is evaluated. The perturbation analysis is validated by the comparison between our numerical and experimental data. This study provides an effective method for the nonlinear dynamic design of suspended microchannel resonators and multi-particle detection.

Keywords Resonator, Nonlinear dynamics, Inverse problem, Primary resonance, Method of multiple scales, Mass detection

1 Introduction

Micro/nano resonators are the core components in micro/nano electromechanical systems (MEMS/NEMS) for converting electrical energy into mechanical energy or mechanical energy into electrical energy [1–3]. Owing to their simple structure, small mass, high quality factor, and ease of actuation [4–6], they are often employed as sensors to detect the analytes such as micro/nano particles [7], biomolecules [8], weak forces [9], and temperature [10]. However, for analytes that need to be detected in liquid environments, such as cells [11], viruses [12], and proteins [13], the viscosity of the liquid severely reduces the quality factor of the resonator, making detection difficult [14]. To address this issue, Burg et al. [15] proposed a new type of resonator called the suspended microchannel resonator (SMR). A fluidic channel is integrated inside the SMR, which significantly reduces the viscous dissipation caused by the liquid and improves the quality factor by four orders of magnitude compared with conventional resonators, thereby enabling highly sensitive detection in liquid environments [16].

To further exploit the applications of SMRs in biology, medicine, and chemical engineering, extensive theoretical investigations have been conducted on such micro/nano structures with internal fluid flow. Zhong et al. [17] derived the solid–liquid coupling governing equations for a fluid-conveying microresonator under thermoelastic damping, and it was shown that the flow velocity significantly increases thermoelastic damping. Yan et al. [18] established a theoretical model to study the dynamic behavior of an electrostatically actuated fluid-conveying microbeam and discussed the effects of flow velocity and viscosity on energy dissipation mechanisms. Subsequently, Yan et al. [19] investigated the pull-in instability and flow-induced flutter of electrostatically actuated SMRs. Dai et al. [20] proposed a nonlinear model of an electrostatically actuated SMR and obtained the numerical results for chaotic divergence. It should be noted that the dimensions of SMRs are at the micro/nano scale. Therefore, incorporating size-dependent theories such as modified couple stress

theory into theoretical modeling is more accurate than directly employing classical continuum mechanics [21–23]. Hu et al. [24] developed a nonlinear model for microbeams conveying fluid based on the modified couple stress theory, and it was indicated that the size effects can enhance structural stability. Deng et al. [25] analyzed the stability and critical flow velocity for the instability of microscale fluid-conveying pipes made of functionally graded materials by using the modified couple stress theory. Zhang et al. [26] employed the invariant manifold approach to study the nonlinear free vibration behavior of fluid-conveying microtubes reinforced by graphene sheets, and the modified couple stress theory was introduced to account for the size effects.

Huge experimental efforts on mass detection by using SMRs have also been infused. SMRs are mostly operated in the dynamic mode in experiments, where the mass of an analyte is inferred from the resonance frequency shift that is induced by its inertial effects inside the channel [27–29]. Weng et al. [30] fabricated a capture dock at the tip of an SMR to achieve mechanical trapping of cells, eliminating the influence of cell position uncertainty on the resonance frequency. Khan et al. [31] produced a transparent SMR that allows a visual inspection of bubbles, blockages, or residues inside the channel. Olcum et al. [32] proposed a method to track resonance frequency shifts of multiple modes of an SMR, enabling real-time detection of the mass and position of flowing nanoparticles. Katsikis et al. [33] proposed a rotational dynamics method to measure the volume and density of rigid particles inside an SMR, in which the accuracy of the measurements depends on a sufficiently high oscillatory Reynolds number. Recently, Martín-Pérez and Ramos [34] demonstrated that applying hydrostatic pressure inside an SMR can simultaneously modulate the mass detection limit and amplify the buoyant mass differences between similar cell lines. Although fruitful results have been achieved in mass detection by using SMRs, the research on mass detection under nonlinear vibration of the resonator remains relatively limited.

Unlike linear vibration, a resonator actuated into a nonlinear vibration regime exhibits complex frequency responses but offers the improved frequency stability and

measurement resolution [35–37]. Nguyen et al. [38] proposed a bifurcation-based mass detection method, showing that an abrupt amplitude jump is beneficial for enhancing detection sensitivity. The work of Antonio et al. [39] demonstrated that excitation of internal resonance can improve the frequency stability of a nonlinear self-sustained resonator. Subsequently, Wang and Zhang [40] proposed a new method for the detection of single-particle position and mass based on the 1:3 internal resonance between the first two modes of a resonator. Moreover, Olcum et al. [41] found that a resonator actuated in the nonlinear regime can reduce frequency noise and improve the signal-to-noise ratio. For beam-based SMRs driven into a nonlinear regime, one main source of nonlinearities is the geometric nonlinearity. Specifically, the geometric nonlinearity of a doubly clamped beam arises from mid-plane stretching [42–44], while that of a cantilever beam arises from curvature nonlinearity [24,45]. Both introduce a hardening cubic nonlinear term into the governing equations. When the resonator is electrostatically actuated, an additional term related to a softening electrostatic nonlinearity appears in the governing equation [46]. The hardening effect of geometric nonlinearity and the softening effect of electrostatic nonlinearity compete with each other, which impacts the mechanical behavior of electrostatically actuated SMRs.

In the present work, a model of the electrostatically actuated SMRs is established, which incorporates both the geometric and electrostatic nonlinearities. The effects of these two nonlinear mechanisms on the SMRs are discussed. Subsequently, a method for particle detection by using nonlinear frequency shifts is proposed. The examples for identifying a single particle and two particles are presented, which illustrates the capability of the proposed method to identify multiple particles with different masses. The robustness of the particle identification method is verified by considering the Gaussian white noise. Finally, the method is validated by comparing the experimental and numerical results.

2 Model development

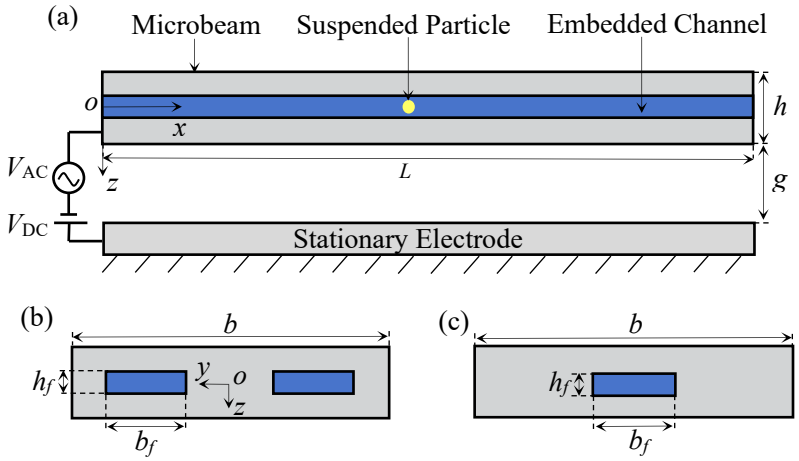


Fig. 1 Schematic diagram of the SMR. (a) Electrostatically actuated SMR with a single suspended particle. (b) Cross-section of the cantilevered SMR. (c) Cross-section of the doubly clamped SMR.

The schematic diagram of an electrostatically actuated SMR is shown in Fig. 1. The resonator is modeled as a microbeam containing an internal fluidic channel, as illustrated in Fig. 1(a). The length, width, and thickness of the beam are denoted as L, b and h, respectively. The length, width, and height of the internal fluidic channel are represented as L, b_f and h_f, respectively. Electrostatic actuation is provided by a fixed electrode located with a gap distance g from the resonator, and the electrostatic driving force is given as the combination of a DC polarization voltage V_{DC} and a harmonic AC voltage V_{AC}. Two types of microbeam resonators are considered here: the cantilever and the doubly clamped beam. The doubly clamped beam offers a high resonance frequency and high sensitivity [47, 48]. In contrast, the cantilever is clamped at one end only. This configuration suffers less clamping loss, resulting in a low energy dissipation and thus a high quality factor [49, 50]. For the cantilevered SMR, the internal channel is U-shaped, guiding fluid from the clamped end to the free end and back. The cross-sectional view is shown in Fig. 1(b). For the doubly clamped SMR, the internal channel is straight, and fluid is conveyed from one end to the other. The cross-section is shown in Fig. 1(c).

2.1 The cantilevered SMR

Hamilton's principle is adopted to establish the governing equations of the cantilevered SMR, and the mathematical formulation is presented as follows:

$$\delta\int_{t_1}^{t_2}\left(T-U+W\right)dt=0, \tag{1}$$

where T, U, W are the kinetic, potential energies of the system, and the work done by the electrostatic force, respectively. For the identification of a particle, its flow velocity in the SMR is typically on the order of mm/s [32]. In this case, the suspended particle moves only about 10^{-2} μm per vibration cycle, which is much smaller than the length of the microbeam SMR [32]. Therefore, the effect of flow velocity on the SMR can be negligible [51]. Introducing a curvilinear coordinate s along the length of the cantilevered SMR, the kinetic energy is written as:

$$T=\frac{1}{2}\left(m+M+\sum_{p=1}^{P}\delta_D(s-s_p)m_p\right)\int_0^L\left(\frac{\partial w}{\partial t}\right)^2 ds, \tag{2}$$

where m, M, w, P and s_p are the mass per unit length of the microbeam, the mass per unit length of the internal fluid, the deflection along the z-direction, the total number of suspended particles, and the position of the particle, respectively. The buoyant mass m_p of a particle is defined as follows [51]:

$$m_p=(\rho_p-p_f)V_p, \tag{3}$$

where ρ_p, ρ_f, and V_p are particle density, fluid density, and particle volume, respectively. Since the size of a particle is very small compared with that of a resonator, particles are modeled as concentrated masses characterized by the Dirac delta function δ_D [7].

The modified couple stress theory incorporates a single material length scale parameter l to characterize the influence of size effects in materials [52, 53]. Accordingly, the strain energy of the SMR with the modified couple stress theory is expressed as [24]:

$$U=\frac{1}{2}\int_0^L\left(EI+GAl^2\right)\kappa^2 ds, \tag{4}$$

where E, I, G, A, and κ are the elasticity modulus, the second moment of area, the shear modulus, the cross-sectional area, and the curvature of the centerline, respectively. Under the assumption of an inextensible cantilevered SMR, the curvature is expressed as follows [54]:

$$\kappa = \frac{\partial^2 w / \partial s^2}{\sqrt{1-\left(\partial w / \partial s\right)^2}}. \tag{5}$$

The electrostatic work is given as follows [39, 54]:

$$W = \int_0^L \int_0^w \frac{\varepsilon_0 b\left[V_{DC} + V_{AC}\cos\left(\Omega t\right)\right]^2}{2\left(g-\zeta\right)^2} d\zeta ds, \tag{6}$$

where $\varepsilon_0 = 8.854\times10^{-12}$ $C^2N^{-1}m^{-2}$ is the permittivity of the gap space medium [55], Ω is the excitation frequency. By substituting Eqs. (2), (4), and (6) into Eq. (1) and setting the viscous damping coefficient to C_d, the governing equation and boundary conditions of the cantilevered SMR are obtained:

$$\begin{aligned}&\left(EI+GAl^2\right)\left[\frac{\partial^4 w}{\partial s^4}+\frac{\partial^4 w}{\partial s^4}\left(\frac{\partial w}{\partial s}\right)^2+4\frac{\partial w}{\partial s}\frac{\partial^2 w}{\partial s^2}\frac{\partial^3 w}{\partial s^3}+\left(\frac{\partial^2 w}{\partial s^2}\right)^3\right]\\ &+(m+M)\frac{\partial^2 w}{\partial t^2}+\sum_{p=1}^{P}\delta_D(s-s_p)m_p\frac{\partial^2 w}{\partial t^2}+C_d\frac{\partial w}{\partial t}=\frac{\varepsilon_0 b\left[V_{DC}+V_{AC}\cos\left(\Omega t\right)\right]^2}{2\left(g-w\right)^2},\end{aligned} \tag{7}$$

$$w\big|_{s=0}=0,\ \left.\frac{\partial w}{\partial s}\right|_{s=0}=0,\ \left.\frac{\partial^2 w}{\partial s^2}\right|_{s=L}=0,\ \left.\frac{\partial^3 w}{\partial s^3}\right|_{s=L}=0. \tag{8}$$

The following dimensionless parameters are introduced:

$$\begin{aligned}&\hat{w}=\frac{w}{g},\ \hat{t}=t\sqrt{\frac{EI}{\left(m+M\right)L^4}},\ \hat{\Omega}=\Omega\sqrt{\frac{\left(m+M\right)L^4}{EI}},\ \xi=\frac{s}{L},\ \mu=\frac{GAl^2}{EI},\\ &c=\frac{C_d L^2}{\sqrt{\left(m+M\right)EI}},\ \alpha_1=\frac{g^2}{L^2},\ \alpha_2=\frac{\varepsilon_0 bL^4}{2g^3EI},\ \beta_p=\frac{m_p}{\left(m+M\right)L}.\end{aligned} \tag{9}$$

By substituting Eq. (9) into Eqs. (7) and (8) and removing the hat notation, the dimensionless governing equation and boundary conditions are obtained as follows:

$$\begin{aligned}&\left(1+\mu\right)w''''+\left(1+\mu\right)\alpha_1\left[w''''w'^2+4w'w''w'''+w''^3\right]\\ &+\left[1+\sum_{p=1}^{P}\beta_p\delta_D(\xi-\xi_p)\right]\ddot{w}+c\dot{w}=\alpha_2\frac{\left[V_{DC}+V_{AC}\cos\left(\Omega t\right)\right]^2}{\left(1-w\right)^2},\end{aligned} \tag{10}$$

$$w\big|_{\xi=0}=0,\ w'\big|_{\xi=0}=0,\ w''\big|_{\xi=1}=0,\ w'''\big|_{\xi=1}=0, \tag{11}$$

where the primes represent $\partial(\,)/\partial\xi$ and the dots represent $\partial(\,)/\partial t$.

To obtain the nonlinear response of the SMR under primary resonance excitation, the method of multiple scales is used to derive an approximate analytical solution. The time scales and time derivatives are defined as follows:

$$T_0=t,\ T_1=\varepsilon t,\ T_2=\varepsilon^2 t,\ D_0=\frac{\partial}{\partial T},\ D_1=\frac{\partial}{\partial T_1},\ D_2=\frac{\partial}{\partial T_2}. \tag{12}$$

where ε is the bookkeeping parameter. The solution to the governing Eq. (10) is assumed to consist of the static and dynamic parts [40, 46]:

$$w(\xi,\ t;\ \varepsilon)=w_s(\xi)+w_d(\xi,t;\varepsilon)=w_s(\xi)+\sum_{i=1}^{3}\varepsilon^i w_i\left(\xi,T_0,T_2\right). \tag{13}$$

The damping and excitation are rescaled as $c=\varepsilon^2 c$ and $V_{\mathrm{AC}}=\varepsilon^3 V_{\mathrm{AC}}$ [40, 46]. By substituting Eqs. (12) and (13) into Eqs. (10) and (11), the following equations are obtained by expanding the electrostatic force term into the Taylor series:

Order ε^0:

$$(1+\mu)w_s''''+\alpha_1(1+\mu)\left(w_s''''w_s'^2+4w_s'w_s''\,w_s'''+w_s''^3\right)=\frac{\alpha_2 V_{\mathrm{DC}}^2}{(1-w_s)^2}. \tag{14}$$

The static deflection is obtained by solving Eq. (14), and the corresponding boundary conditions are:

$$w_s\big|_{\xi=0}=0,\ w_s'\big|_{\xi=0}=0,\ w_s''\big|_{\xi=1}=0,\ w_s'''\big|_{\xi=1}=0. \tag{15}$$

Order ε^1:

$$\Gamma(w_1)=0, \tag{16}$$

where

$$\begin{aligned}\Gamma(w_i)=&\left[1+\sum_{p=1}^{P}\beta_p\delta_D(\xi-\xi_p)\right]D_0^2 w_i-\frac{2\alpha_2 V_{\mathrm{DC}}^2}{(1-w_s)^3}w_i+(1+\mu)w_i''''\\&+\alpha_1(1+\mu)\left(2w_s''''w_s'w_i'+w_i''''w_s'^2+4w_s'w_i''w_s'''+4w_s'w_s''\,w_i'''+4w_i'w_s''\,w_s'''+3w_s''^2w_i''\right).\end{aligned} \tag{17}$$

Order ε^2:

$$\begin{aligned}\Gamma(w_2)=&-\alpha_1(1+\mu)\left(w_s''''w_1'^2+2w_1'''w_s'w_1'+4w_s'w_1''\,w_1'''+4w_1'w_1''\,w_s'''\right)\\&-\alpha_1(1+\mu)\left(4w_1'w_s''\,w_1'''+3w_s''\,w_1''^2\right)+\frac{3\alpha_2 V_{\mathrm{DC}}^2}{(1-w_s)^4}w_1^2.\end{aligned} \tag{18}$$

Order ε^3:

$$\begin{aligned}\Gamma(w_3) = &-2\left[1+\sum_{p=1}^{P}\beta_p\delta_D(\xi-\xi_p)\right]D_0D_2w_1 - cD_0w_1 + \frac{6\alpha_2V_{\mathrm{DC}}^2}{(1-w_s)^4}w_1w_2 \\ &+\frac{4\alpha_2V_{\mathrm{DC}}^2}{(1-w_s)^5}w_1^3 - \alpha_1(1+\mu)\left(2w_s''''w_1'w_2' + w_1''''w_1'^2 + 2w_1''''w_s'w_2'\right) \\ &-\alpha_1(1+\mu)\left(2w_2''''w_s'w_1' + 4w_s'w_2''\,w_1''' + 4w_s'w_1''\,w_2''' + 4w_1'w_2''\,w_s'''\right) \\ &-\alpha_1(1+\mu)\left(4w_1'w_1''\,w_1''' + 4w_1'w_s''\,w_2''' + 4w_2'w_1''\,w_s''' + 4w_2'w_s''\,w_1'''\right) \\ &-\alpha_1(1+\mu)\left(w_1''^3 + 6w_s''\,w_1''w_2''\right) + \frac{2\alpha_2V_{\mathrm{DC}}V_{\mathrm{AC}}\cos(\Omega t)}{(1-w_s)^2}.\end{aligned} \tag{19}$$

The boundary conditions for Eqs. (16), (18) and (19) are:

$$w_i\big|_{\xi=0} = 0,\ w_i'\big|_{\xi=0} = 0,\ w_i''\big|_{\xi=1} = 0,\ w_i'''\big|_{\xi=1} = 0,\ i = 1,\ 2,\ 3. \tag{20}$$

The eigenvalue problem of the SMR is formulated by Eqs. (16) and (20). When the effect of damping is considered, only the homogeneous solutions of the directly excited mode is taken into account [40, 46]. Therefore, the solution to Eq. (16) in conjunction with Eq. (20) is assumed as follows:

$$w_1(\xi, T_0, T_2) = \phi(\xi)A(T_2)\mathrm{e}^{i\omega T_0} + \phi(\xi)\overline{A}(T_2)\mathrm{e}^{-i\omega T_0}, \tag{21}$$

where ϕ and ω are the mode shape and natural frequency of the directly excited cantilever mode [7, 24], A is the complex function to be determined, and $\overline{A}$ is its complex conjugate. By substituting Eq. (21) into Eq. (18), the following is obtained:

$$\Gamma(w_2) = \left(A^2\mathrm{e}^{2i\omega T_0} + 2A\overline{A} + \overline{A}^2\mathrm{e}^{-2i\omega T_0}\right)h(\xi), \tag{22}$$

where

$$\begin{aligned}h(\xi) = &-\alpha_1(1+\mu)\left(w_s''''\phi'^2 + 2w_s'\phi'''\phi' + 4w_s'\phi''\phi''' + 4w_s'''\phi'\phi''\right) \\ &-\alpha_1(1+\mu)\left(4w_s''\,\phi'\phi''' + 3w_s''\,\phi''^2\right) + \frac{3\alpha_2V_{\mathrm{DC}}^2}{(1-w_s)^4}\phi^2.\end{aligned} \tag{23}$$

A particular solution to Eqs. (20) and (22) is given by:

$$w_2(\xi, T_0, T_2) = \psi_1(\xi)A^2(T_2)\mathrm{e}^{2i\omega T_0} + 2\psi_2(\xi)A\overline{A} + \psi_1(\xi)\overline{A}^2\mathrm{e}^{-2i\omega T_0}, \tag{24}$$

where ψ_1 and ψ_2 are determined by the following equations:

$$h(\xi)=(1+\mu)\psi_1''''-4\omega^2\psi_1\left[1+\sum_{p=1}^{P}\beta_p\delta_D(\xi-\xi_p)\right]-\frac{2\alpha_2V_{\mathrm{DC}}^2}{(1-w_s)^3}\psi_1$$
$$+\alpha_1(1+\mu)\left(2w_s''''w_s'\psi_1'+\psi_1''''w_s'^2+4w_s'\psi_1''w_s'''+4w_s'w_s''\ \psi_1'''\right) \tag{25}$$
$$+\alpha_1(1+\mu)\left(4\psi' w_s''\ w_s'''+3w_s''^2\psi_1''\right),$$

$$h(\xi)=\alpha_1(1+\mu)\left(2w_s''''w_s'\psi_2'+\psi_2''''w_s'^2+4w_s'\psi_2''\ w_s'''+4w_s'w_s''\ \psi_2'''\right)$$
$$+\alpha_1(1+\mu)\left(4\psi_2'w_s''\ w_s'''+3w_s''^2\psi_2''\right) \tag{26}$$
$$(1+\mu)\psi_2''''-\frac{2\alpha_2V_{\mathrm{DC}}^2}{(1-w_s)^3}\psi_2,$$

$$\psi_j\big|_{\xi=0}=0,\ \psi_j'\big|_{\xi=0}=0,\psi_j''\big|_{\xi=1}=0,\ \psi_j'''\big|_{\xi=1}=0,\ j=1,2. \tag{27}$$

A detuning parameter σ is introduced to describe the closeness between the excitation frequency Ω and the natural frequency ω:

$$\Omega=\omega+\varepsilon^2\sigma. \tag{28}$$

By substituting Eqs. (21), (24), and (28) into Eq. (19), the following expressions are derived:

$$\Gamma(w_3)=-2i\omega\frac{\partial A}{\partial T_2}\left[1+\sum_{p=1}^{P}\beta_p\delta_D(\xi-\xi_p)\right]\phi\mathrm{e}^{i\omega T_0}-i\omega cA\phi\mathrm{e}^{i\omega T_0}+\chi(\xi)A^2\bar{A}\mathrm{e}^{i\omega T_0}$$
$$+\chi_F(\xi)\mathrm{e}^{i(\omega T_0+\sigma T_2)}+\mathrm{cc}+\mathrm{NST}, \tag{29}$$

$$\chi(\xi)=\chi_q^G(\xi)+\chi_c^G(\xi)+\chi_q^E(\xi)+\chi_c^E(\xi),\ \chi_F(\xi)=\frac{\alpha_2V_{\mathrm{DC}}V_{\mathrm{AC}}}{(1-w_s)^2}, \tag{30}$$

$$\begin{aligned}\chi_q^G(\xi)=&-\alpha_1(1+\mu)\left(2w_s''''\phi'\psi_1'+4w_s''''\phi'\psi_2'+4w_s'\phi''''\psi_2'+2w_s'\phi''''\psi_1'+2w_s'\phi'\psi_1''''\right)\\&-\alpha_1(1+\mu)\left(4w_s'\phi'\psi_2''''+4w_s'\phi'''\psi_1''+8w_s'\phi'''\psi_2''+8w_s'\phi''\psi_2'''+4w_s'\phi''\psi_1'''\right)\\&-\alpha_1(1+\mu)\left(8w_s'''\phi'\psi_2''+4w_s'''\phi'\psi_1''+8w_s''\ \phi'\psi_2'''+4w_s''\ \phi'\psi_1'''+8w_s'''\phi''\psi_2'\right)\\&-\alpha_1(1+\mu)\left(4w_s'''\phi''\psi_1'+8w_s''\ \phi'''\psi_2'+4w_s''\ \phi'''\psi_1'+12w_s''\ \phi''\psi_2''+6w_s''\ \phi''\psi_1''\right),\end{aligned} \tag{31}$$

$$\chi_c^G(\xi)=-\alpha_1(1+\mu)\left(3\phi''''\phi'^2+3\phi''^3+12\phi'\phi''\phi'''\right), \tag{32}$$

$$\chi_q^E(\xi)=\frac{6\alpha_2V_{\mathrm{DC}}^2}{(1-w_s)^4}\left(2\phi\psi_2+\phi\psi_1\right),\ \chi_c^E(\xi)=\frac{12\alpha_2V_{\mathrm{DC}}^2}{(1-w_s)^5}\phi^3. \tag{33}$$

In Eq. (29), cc and NST stand for the complex conjugate and non-secular terms, respectively. In Eq. (30), the quadratic and cubic terms from geometric nonlinearity are χ_q^G and χ_c^G, and those from electrostatic nonlinearity are χ_q^E and χ_c^E. To derive

a uniform approximation of the dynamic deflection, the right-hand side of Eq. (29) is multiplied by $\phi e^{-i\omega T_0}$ and then integrated over $\xi \in [0, 1]$, which yields the solvability condition [40, 46]:

$$2i\omega \frac{\partial A}{\partial T_2}\left[1+\sum_{p=1}^{P}\beta_p\phi^2\left(\xi_p\right)\right]+i\omega\eta A-SA^2\bar{A}-Fe^{i\sigma T_2}=0, \tag{34}$$

where

$$\eta=\int_0^1 c\phi^2 d\xi,\ S=\int_0^1 \chi\phi d\xi,\ F=\int_0^1 \chi_F\phi d\xi. \tag{35}$$

For low damping, η can be calculated from the quality factor Q as $\eta=\omega/2Q$ [46]. The complex function A can be written in polar form as $A=(1/2)ae^{i\beta}$, where the real-valued functions a and β correspond to the amplitude and phase, respectively. By substituting A into Eq. (34) and separating the real and imaginary parts, the following results are obtained:

$$\frac{\partial a}{\partial T_2}\left[1+\sum_{p=1}^{P}\beta_p\phi^2\left(\xi_p\right)\right]=-\frac{1}{2}\eta a+\frac{F}{\omega}\sin\gamma, \tag{36}$$

$$a\frac{\partial \gamma}{\partial T_2}\left[1+\sum_{p=1}^{P}\beta_p\phi^2\left(\xi_p\right)\right]=a\sigma\left[1+\sum_{p=1}^{P}\beta_p\phi^2\left(\xi_p\right)\right]+\frac{Sa^3}{8\omega}+\frac{F}{\omega}\cos\gamma, \tag{37}$$

where $\gamma=\sigma T_2-\beta$. By substituting Eqs. (21) and (24) into Eq. (13), a uniform second-order approximation to the dynamic deflection of the SMR is derived：

$$w_d=a\cos\left(\Omega t-\gamma\right)\phi+\frac{1}{2}a^2\left[\psi_2+\cos 2\left(\Omega t-\gamma\right)\psi_1\right]. \tag{38}$$

The fixed-point conditions of the system are obtained by setting $\partial a/\partial T_2=0$ and $\partial\gamma/\partial T_2=0$ in Eqs. (36) and (37). The frequency-response equation is then derived by eliminating γ:

$$\frac{a^2\eta^2}{4}+\left\{a\sigma\left[1+\sum_{p=1}^{P}\beta_p\phi^2\left(\xi_p\right)\right]+\frac{Sa^3}{8\omega}\right\}^2=\frac{F^2}{\omega^2}. \tag{39}$$

The stability of the fixed points can be assessed by examining the eigenvalues of the corresponding Jacobian matrix [56].

2.2 The doubly clamped SMR

Unlike the geometric nonlinearity caused by curvature in a cantilevered SMR, the geometric nonlinearity of a doubly clamped SMR originates from the mid-plane stretching as seen in the term of $\left(EA/2L\right)\int_0^L\left(\partial w/\partial x\right)^2 dx$ in Eq. (40). The governing equation of the doubly clamped SMR under electrostatic actuation is given by [7, 57]:

$$\begin{aligned}\left(EI+GAl^2\right)\frac{\partial^4 w}{\partial x^4}-\left[N_f+\frac{EA}{2L}\int_0^L\left(\frac{\partial w}{\partial x}\right)^2 dx\right]\frac{\partial^2 w}{\partial x^2}+(m+M)\frac{\partial^2 w}{\partial t^2}\\ +\sum_{p=1}^{P}\delta_D(x-x_p)m_p\frac{\partial^2 w}{\partial t^2}+C_d\frac{\partial w}{\partial t}=\frac{\varepsilon_0 b\left[V_{DC}+V_{AC}\cos\left(\Omega t\right)\right]^2}{2\left(g-w\right)^2},\end{aligned} \tag{40}$$

where N_f is the axial load, with positive values indicating tension and negative values indicating compression. The boundary conditions for the doubly clamped SMR are:

$$w\big|_{x=0}=0,\ \left.\frac{\partial w}{\partial x}\right|_{x=0}=0,\ w\big|_{x=L}=0,\ \left.\frac{\partial w}{\partial x}\right|_{x=L}=0. \tag{41}$$

By substituting $\hat{x}=x/L$ and Eq. (9) into Eqs. (40) and (41) and removing the hat notation, the dimensionless governing equation and boundary conditions are derived:

$$\begin{aligned}\left(1+\mu\right)\frac{\partial^4 w}{\partial x^4}-\left[N_F+\alpha_3\int_0^L\left(\frac{\partial w}{\partial x}\right)^2 dx\right]\frac{\partial^2 w}{\partial x^2}+\left[1+\sum_{p=1}^{P}\beta_p\delta_D(x-x_p)\right]\frac{\partial^2 w}{\partial t^2}\\ +c\frac{\partial w}{\partial t}=\alpha_2\frac{\left[V_{DC}+V_{AC}\cos\left(\Omega t\right)\right]^2}{\left(1-w\right)^2},\end{aligned} \tag{42}$$

$$w\big|_{x=0}=0,\ \left.\frac{\partial w}{\partial x}\right|_{x=0}=0,\ w\big|_{x=1}=0,\ \left.\frac{\partial w}{\partial x}\right|_{x=1}=0. \tag{43}$$

The two dimensionless parameters of N_F and α_3 as given in Eq. (42) are defined as follows:

$$N_F=\frac{N_f L^2}{EI},\alpha_3=\frac{Ag^2}{2I}. \tag{44}$$

The other dimensionless parameters in Eq. (42) are given in Eq. (9). Again, the multiscale method is applied to the governing equation to obtain an approximate analytical solution for the primary resonance of the doubly clamped SMR. The following modulation equations are derived and the derivation details are in Appendix A:

$$\frac{\partial a}{\partial T_2}\left[1+\sum_{p=1}^{P}\beta_p\varphi^2\left(x_p\right)\right]=-\frac{1}{2}\eta a+\frac{F}{\omega}\sin\gamma, \tag{45}$$

$$a\frac{\partial \gamma}{\partial T_2}\left[1+\sum_{p=1}^{P}\beta_p\varphi^2\left(x_p\right)\right]=a\sigma\left[1+\sum_{p=1}^{P}\beta_p\varphi^2\left(x_p\right)\right]+\frac{\Lambda a^3}{8\omega}+\frac{F}{\omega}\cos\gamma, \tag{46}$$

where Λ is the nonlinear coefficient of the system, and φ is the mode shape of the clamped-clamped beam [7]. The frequency-response equation is then obtained by setting $\partial a/\partial T_2=0$ and $\partial \gamma/\partial T_2=0$:

$$\frac{a^2\eta^2}{4}+\left\{a\sigma\left[1+\sum_{p=1}^{P}\beta_p\varphi^2\left(x_p\right)\right]+\frac{\Lambda a^3}{8\omega}\right\}^2=\frac{F^2}{\omega^2}. \tag{47}$$

3 Results and discussion

3.1 Influence of parameters on the dynamics

The parameters of the SMR under consideration are as follows: the width b = 10 μm, the thickness h = 1 μm, the initial gap g = 1 μm，the Poisson's ratio v = 0.3, and the elasticity modulus E = 169 GPa [58]. The internal channel is characterized by a width b_f = 2 μm and a height h_f = 600 nm.

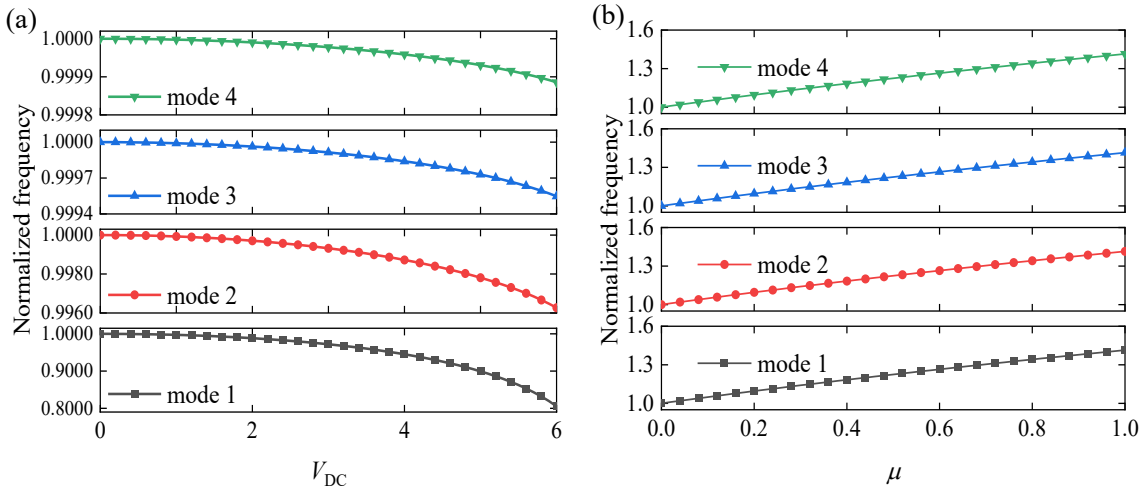


Fig. 2 Effects of polarization voltage V_{DC} (a) and scale parameter μ (b) on the normalized frequencies of the cantilevered SMR, where the beam length is $L = 10b$.

The effects of the polarization voltage V_{DC} and the scale parameter μ on the normalized frequencies of the cantilevered SMR are shown in Fig. 2(a–b). The normalized frequencies of the beam are obtained by dividing each natural frequency by the corresponding value at $V_{DC} = 0$ and $\mu = 0$. As observed in Fig. 2(a), the first four normalized resonance frequencies decrease with increasing V_{DC}, and higher-order modes are less affected. This is primarily attributed to the enhanced softening effect of the electrostatic force caused by a larger V_{DC}, which reduces the effective stiffness of the system and consequently lowers the frequencies. The softening effect is most pronounced for the first resonance mode and becomes weaker for higher-order modes. From Fig. 2(b), it is seen that the first four normalized resonance frequencies increase with μ, and the increments are similar across all modes. This behavior is explained by the increase in the effective stiffness of the system due to a larger scale parameter μ.

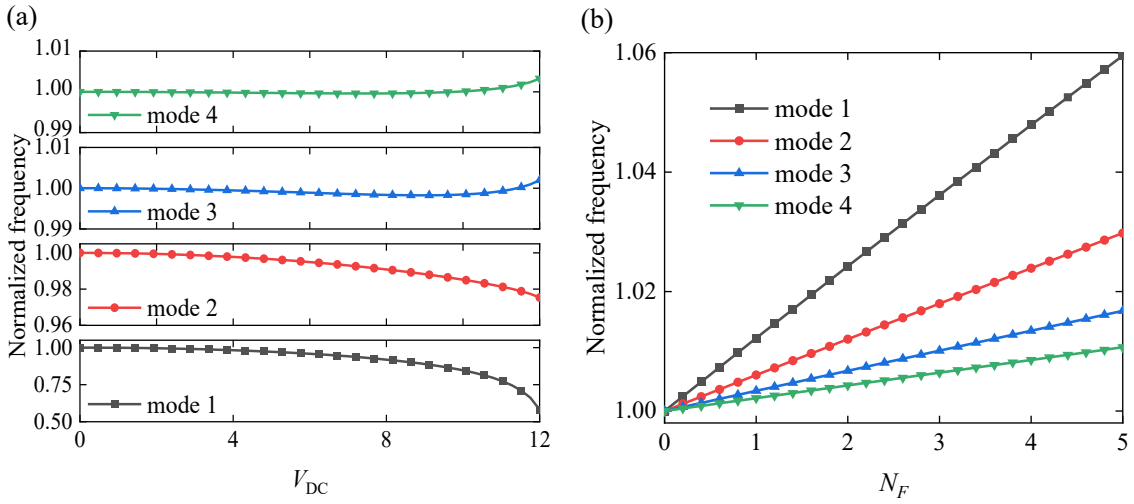


Fig. 3 Effects of polarization voltage V_{DC} (a) and axial load N_F (b) on the normalized frequencies of the doubly clamped SMR, where the beam length is $L = 20b$.

The effects of the polarization voltage V_{DC} and the axial load N_F on the normalized frequencies of the doubly clamped SMR are shown in Fig. 3(a–b). The normalized frequencies of the beam are obtained by dividing each natural frequency by the corresponding value at $V_{DC} = 0$, $\mu = 0$ and $N_F = 0$. As observed in Fig. 3(a), the first two resonance frequencies decrease with increasing V_{DC}. However, for the third

and fourth modes, an increase in the frequencies is observed when V_{DC} exceeds a critical value. This behavior is attributed to the competition between the hardening effect caused by mid-plane stretching and the softening effect of the electrostatic force. In the high V_{DC} regime for the third and fourth modes, the hardening effect becomes dominant, leading to an increase in the effective stiffness, and consequently resulting in higher frequencies. Furthermore, it can be seen from Fig. 3(b) that all normalized frequencies increase with the applied axial load, indicating that a larger axial load enhances the effective stiffness of the structure.

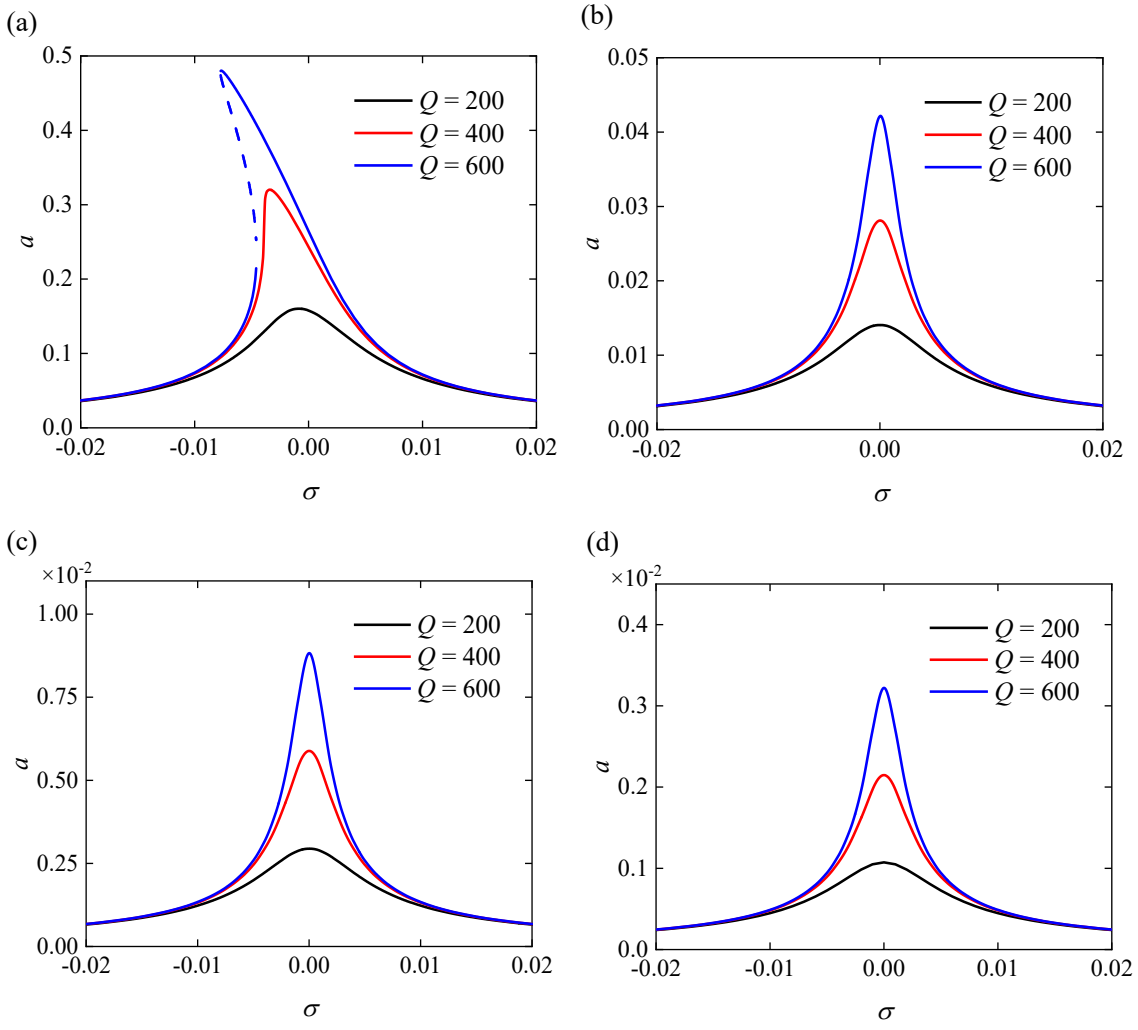


Fig. 4 Variation of the amplitude-frequency responses with the quality factor Q for the first four modes of the cantilevered SMR: (a) first mode, (b) second mode, (c) third mode, (d) fourth mode.

The variation of the amplitude-frequency responses of the first four modes of the

cantilevered SMR with the quality factor Q is shown in Fig. 4(a–d). In the response curves, solid lines denote stable branches, while dashed lines represent unstable branches. The parameters used in Fig. 4 are as follows: $L = 10b$, $\mu = 0.1$, $V_{DC} = 1$, and $V_{AC} = 0.1$. For the first mode, a clear softening behavior is observed in the amplitude-frequency response, i.e., the resonance peak bends toward lower frequencies with increasing vibration amplitude. As Q increases, the softening effect becomes more pronounced: the peak response amplitude increases, and the peak frequency decreases. This phenomenon is attributed to the nonlinear growth of the electrostatic force under parallel-plate actuation. This force generates an equivalent negative stiffness that counteracts the geometric hardening caused by curvature nonlinearity, thereby reducing the overall effective stiffness of the system. For the second, third, and fourth modes, no significant bending is observed in the amplitude-frequency response curves. The main reason is that, under the present excitation, the vibration amplitudes of the higher-order modes are relatively small, making the effects of curvature nonlinearity and electrostatic nonlinearity comparable. Consequently, no dominant hardening or softening behavior is observed.

The influence of the actuation voltage V_{AC} on the amplitude-frequency responses for the first four modes of the cantilevered SMR is shown in Fig. 5(a–d). The parameters used in Fig. 5 are: $L = 10b$, $\mu = 0.1$, and $V_{DC} = 1$. Experimental results show that energy dissipation decreases in higher-order modes of cantilever resonators, leading to higher quality factors Q [59, 60]. Therefore, different quality factors are considered for different modes in Fig. 5. For the first mode, the resonance peak shifts to lower frequencies with increasing V_{AC}, indicating that the softening effect of the electrostatic force is dominant. For the second, third, and fourth modes, the resonance peaks shift to higher frequencies as V_{AC} increases, revealing that the geometric hardening effect becomes dominant.

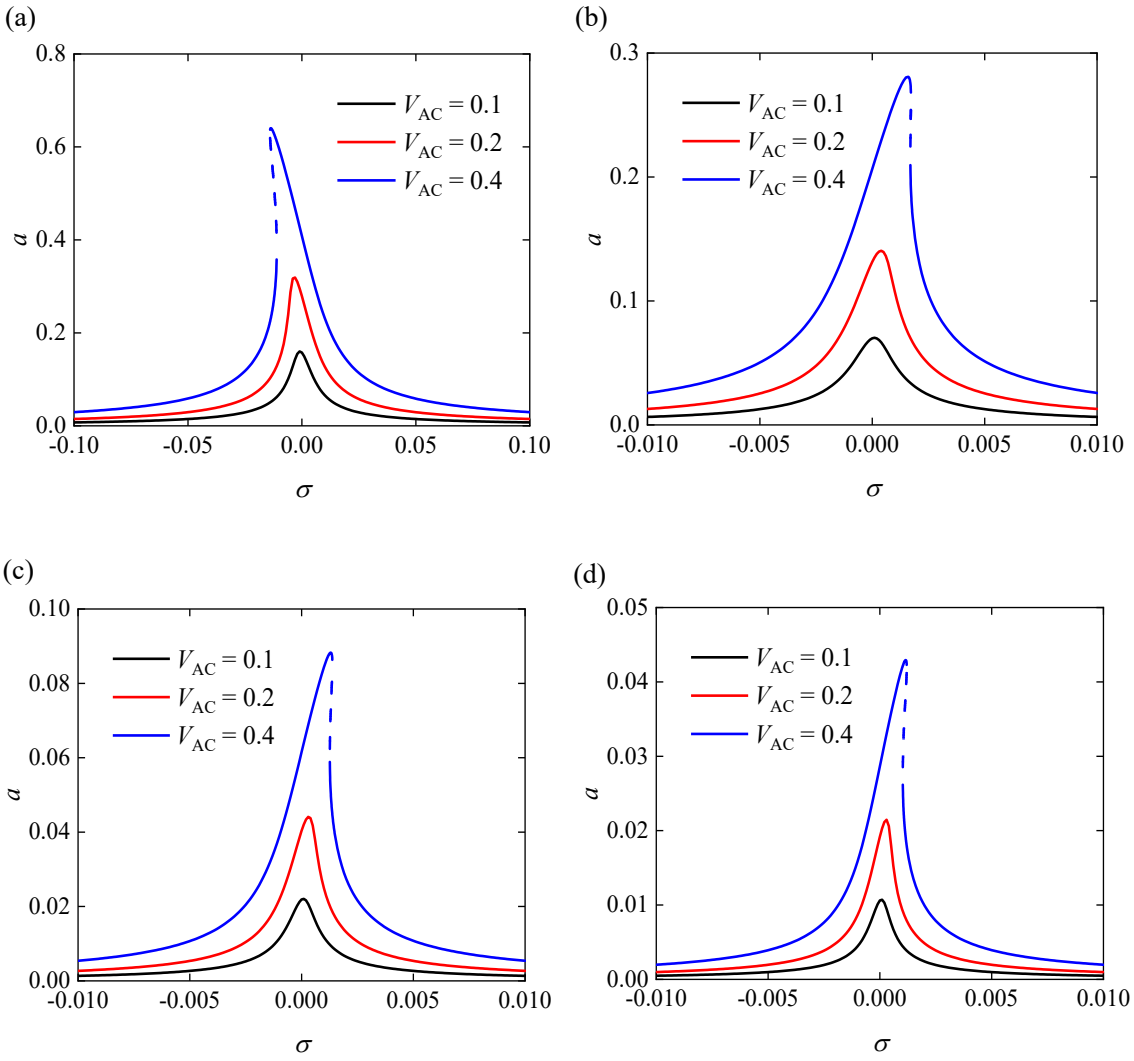


Fig. 5 Variation of the amplitude-frequency responses with the actuation voltage V_{AC} for the first four modes of the cantilevered SMR, each with a different quality factor: (a) first mode with Q = 200, (b) second mode with Q = 1000, (c) third mode with Q = 1500, (d) fourth mode with Q = 2000.

Nonlinear behavior regimes for the first four modes of the cantilevered SMR under nonlinear vibration conditions are presented in Fig. 6(a–d). The red curve represents the pull-in boundary, i.e., the critical voltage leading to electrostatic pull-in failure of the resonator. The yellow region denotes the softening region, where the electrostatic nonlinearity dominates, causing the amplitude-frequency response curve to bend leftward. The gray region denotes the hardening region, where the geometric nonlinearity dominates, causing the amplitude-frequency response curve to bend rightward. For the first vibrational mode in the range $L/b \in [5, 20]$, the softening

region occupies most of the area below the pull-in boundary. This indicates that the softening effect of the electrostatic nonlinearity is more pronounced, while the hardening effect of the geometric nonlinearity remains relatively weak. As the vibrational mode order increases, the proportion of the hardening region increases significantly. In particular, for the fourth mode, the hardening region occupies almost the entire area below the pull-in boundary. This suggests that with increasing mode order, the number of vibration nodes increases, which enhances the curvature variation. Consequently, the hardening effect of the geometric nonlinearity is strengthened and dominates the nonlinear behavior of the SMR.

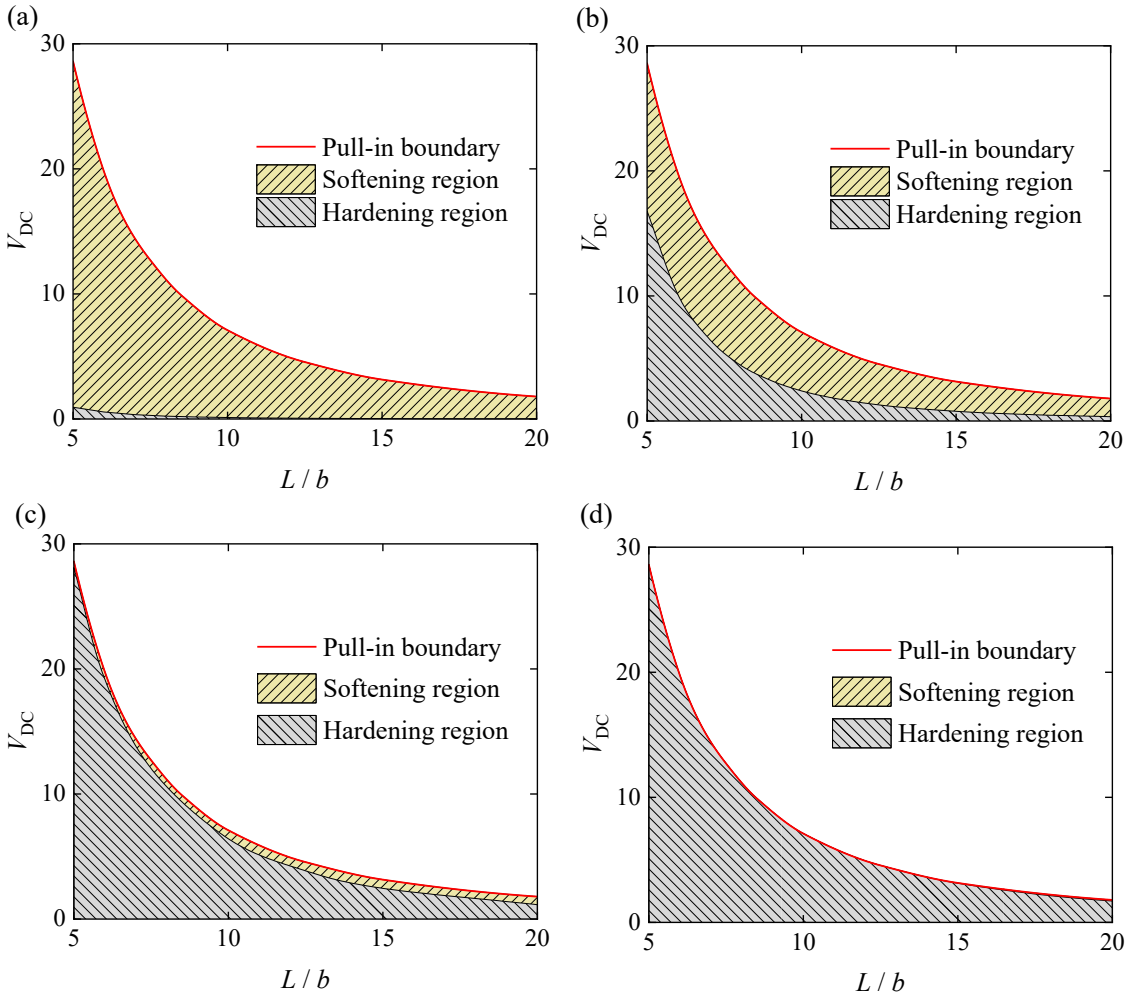


Fig. 6 Nonlinear behavior regimes of the cantilevered SMR for different modes, with $\mu = 0.1$: (a) first mode, (b) second mode, (c) third mode, (d) fourth mode.

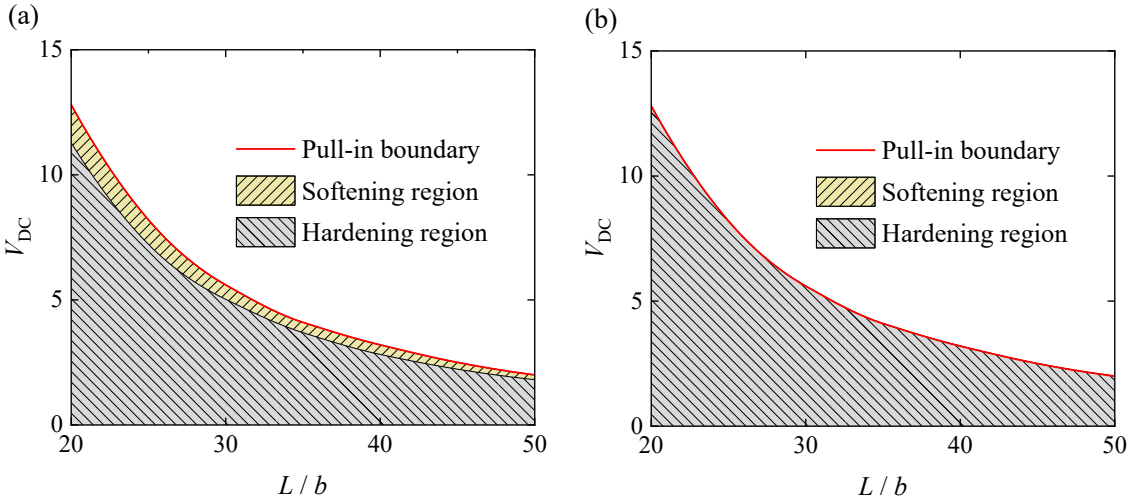


Fig. 7 Nonlinear behavior regimes of the doubly clamped SMR for different modes, with $\mu = 0.1$ and $N_F = 0$: (a) first mode, (b) third mode.

Nonlinear behavior regimes for the doubly clamped SMR are presented in Fig. 7(a–b). The first two symmetric vibration modes, namely the first and third modes, are considered. This is due to the structural symmetry and the use of a symmetric parallel-plate electrostatic actuation, which prevent antisymmetric modes from being effectively excited [46]. For the first mode, the hardening region covers a larger area than the softening region, indicating that the geometric nonlinearity dominates over the electrostatic nonlinearity. The geometric nonlinearity here primarily originates from the mid-plane stretching. For the third mode, the hardening region covers almost the entire area below the pull-in boundary, indicating that the hardening effect of geometric nonlinearity is further enhanced as the mode order increases.

3.2 Mass detection of particles

The detection of particles by using SMRs is mainly performed through two approaches: Adsorption-based detection [15] and flow-through detection [32]. Adsorption-based detection relies on surface functionalization of the internal channel of the SMR to selectively capture [61, 62] and identify particles [63, 64]. Flow-through detection, in contrast, is achieved by measuring the influence of

particles on the SMR frequency during their passage through the channel [65-67], without requiring complex surface modification and without being affected by the change in the effective stiffness of the resonator caused by particle adsorption [68-70]. Therefore, the present work focuses on the flow-through detection method.

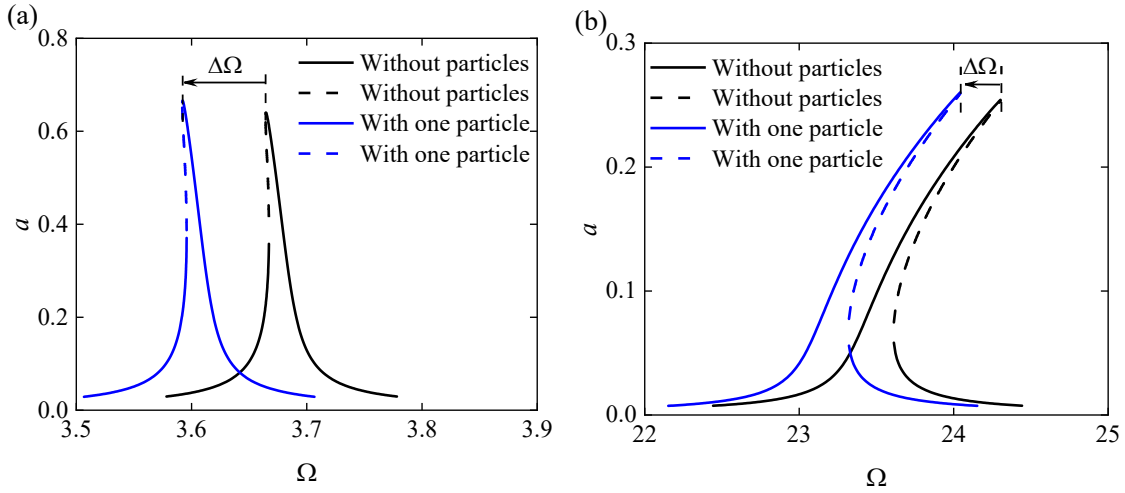


Fig. 8 Effects of a suspended particle on the peak frequencies for the first mode: (a) the cantilevered SMR ($L = 10b$, $\mu = 0.1$, $V_{DC} = 1$, $V_{AC} = 0.4$, $Q = 200$) with a particle of mass $\beta_1 = 1 \times 10^{-2}$ at location $s_p = 0.1$; (b) the doubly clamped SMR ($L = 20b$, $\mu = 0.1$, $N_F = 0$, $V_{DC} = 1$, $V_{AC} = 0.4$, $Q = 200$) with a particle of mass $\beta_1 = 1 \times 10^{-2}$ at location $x_p = 0.5$.

The effects of a single suspended particle on the peak frequencies of the first mode for both the cantilevered SMR and the doubly clamped SMR are illustrated in Figs. 8(a) and (b). For the cantilevered SMR, the resonance peak bends leftward, indicating softening behavior. For the doubly clamped SMR, the resonance peak bends rightward, indicating hardening behavior. Despite the different nonlinear characteristics exhibited by the two types of SMRs, the peak frequencies are shifted in both cases due to the mass effect of the suspended particle. This phenomenon provides a basis for particle mass detection, which can be achieved by monitoring the change in the peak frequency of the SMR. Moreover, it has been shown that particle detection may also be performed by measuring the static deflection of the SMR [71, 72]. However, compared with dynamic frequency-based detection, static deflection offers limited resolution [73, 74] and lower throughput [75, 76].

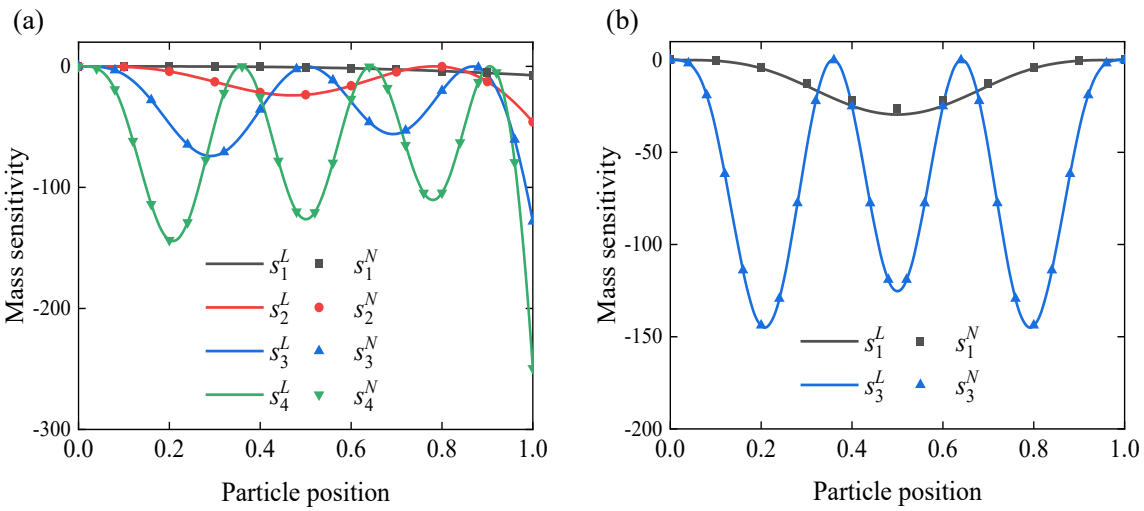


Fig. 9 Comparison of linear and nonlinear mass sensitivity. Linear sensitivity is derived from the resonant frequency shift of the SMR, while nonlinear sensitivity is obtained from the shift of the nonlinear peak frequency. (a) Comparison for the first four modes of the cantilevered SMR (L = 10b, μ = 0.1, V_{DC} = 1, V_{AC} = 0.4, Q = 200) (b) Comparison for the first two symmetric modes of a doubly clamped SMR (L = 20b, μ = 0.1, N_F = 0, V_{DC} = 1, V_{AC} = 0.4, Q = 200)

A comparison between mass sensitivity based on nonlinear peak frequency shifts and that based on linear resonance frequency shifts is presented in Fig. 9(a–b). The nonlinear mass sensitivity is defined as $S_i^N = \Delta\Omega_i/\Delta m$, where S_i^N denotes the nonlinear sensitivity of the i-th mode, $\Delta\Omega_i$ is the peak frequency shift, and Δm is the mass change induced by the suspended particle. The linear mass sensitivity is expressed as $S_i^L = \Delta\omega_i/\Delta m$, with S_i^L being the linear sensitivity for the i-th mode and $\Delta\omega_i$ the linear resonance frequency shift. It can be observed from the Fig. 9 that for the cantilevered SMR, the maximum nonlinear sensitivity occurs when the particle is near the free end, while the sensitivity vanishes at the clamped end and at the nodes of the mode shape. For the doubly clamped SMR, due to structural symmetry, the nonlinear sensitivity is also symmetric with respect to the particle position. For the first mode, the nonlinear sensitivity is zero at the clamped ends and reaches its maximum at the midpoint. For the third mode, the sensitivity is zero at the clamped ends and the internal nodes. Moreover, it is also seen that the difference between nonlinear and linear sensitivities is small, indicating that particle identification by using nonlinear peak frequency shifts does not reduce sensitivity.

In flow-through detection, the positions of particles are altered by the fluid inside the channel [77-79]. Therefore, for mass detection of P particles, both the masses and positions must be identified, which requires at least $2P$ independent frequency shift measurements [80, 81]. For a cantilevered SMR, to perform particle identification with peak frequency shifts, the following expressions are derived from Eq. (39):

$$\begin{cases} 1+\beta_1\phi_1^2(\xi_1)+\beta_2\phi_1^2(\xi_2)+\cdots+\beta_p\phi_1^2(\xi_p)=-\dfrac{S_1F_1^2}{2\omega_1^3\eta^2\sigma_1}, \\ 1+\beta_1\phi_2^2(\xi_1)+\beta_2\phi_2^2(\xi_2)+\cdots+\beta_p\phi_2^2(\xi_p)=-\dfrac{S_2F_2^2}{2\omega_2^3\eta^2\sigma_2}, \\ \vdots \\ 1+\beta_1\phi_{2p}^2(\xi_1)+\beta_2\phi_{2p}^2(\xi_2)+\cdots+\beta_p\phi_{2p}^2(\xi_p)=-\dfrac{S_{2p}F_{2p}^2}{2\omega_{2p}^3\eta^2\sigma_{2p}}. \end{cases} \tag{48}$$

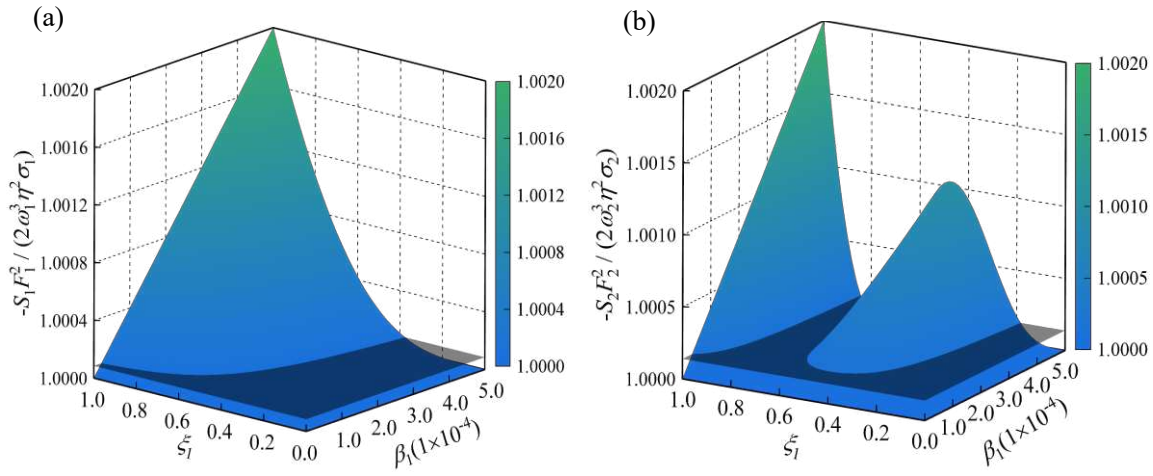
For the doubly clamped beam, the following expressions are obtained by using Eq. (47):

$$\begin{cases} 1+\beta_1\varphi_1^2(x_1)+\beta_2\varphi_1^2(x_2)+\cdots+\beta_p\varphi_1^2(x_p)=-\dfrac{\Lambda_1F_1^2}{2\omega_1^3\eta^2\sigma_1}, \\ 1+\beta_1\varphi_2^2(x_1)+\beta_2\varphi_2^2(x_2)+\cdots+\beta_p\varphi_2^2(x_p)=-\dfrac{\Lambda_2F_2^2}{2\omega_2^3\eta^2\sigma_2}, \\ \vdots \\ 1+\beta_1\varphi_{2p}^2(x_1)+\beta_2\varphi_{2p}^2(x_2)+\cdots+\beta_p\varphi_{2p}^2(x_p)=-\dfrac{\Lambda_{2p}F_{2p}^2}{2\omega_{2p}^3\eta^2\sigma_{2p}}. \end{cases} \tag{49}$$

The right-hand side terms of Eqs. (48) and (49) are obtained from the measured peak frequencies and then substituted into these equations to determine the positions and masses of the particles. In practical particle identification, an array of phase-locked loops (one per vibration mode) can simultaneously track frequency shifts of multiple modes [32].

The identification of a single particle ($\beta_1 = 1.00\times10^{-4}$) inside a cantilevered SMR is illustrated in Fig. 10. It is assumed that the peak frequency shifts obtained from Eq. (39) are consistent with experimental measurements. These frequency results are then substituted into Eq. (48) to determine the particle mass and position. For a particle located at $\xi_1 = 0.600$, the detection results based on the peak frequency shifts of the

first two modes are shown in Fig. 10(a) and (b), respectively. In these figures, the curved surfaces represent the left-hand side of Eq. (48) as a function of the mass β_1 and position ξ_1, while the planes correspond to the right-hand side of Eq. (48) evaluated with the calculated peak frequency shifts. The intersection curves between each surface and the corresponding plane represent the possible pairs of mass and position obtained from the frequency shift of that mode alone. As can be seen from Figs. 10(a) and (b), a single mode yields infinitely many possible identifications. Therefore, to obtain a unique and valid result for the particle mass and position, the intersecting curves from Figs. 10(a) and (b) are projected onto the β_1–ξ_1 plane, leading to Fig. 10(e). The intersection point of the projected curves in Fig. 10(e) (β_1 = 1.00×10^{-4}, $\xi_1 = 0.600$) is the final identification obtained by using the peak frequency shifts of two modes based on Eq. (48). For the particle located at $\xi_1 = 0.850$, the detection results based on the first two modes are presented in Figs. 10(c) and (d), respectively. The projection of the intersection curves from Figs. 10(c) and (d) is shown in Fig. 10(f). Two intersection points are observed in Fig. 10(f): (β_1 = 1.00×10^{-4}, $\xi_1 = 0.850$) and ($\beta_1 = 1.62\times10^{-4}$, $\xi_1 = 0.725$). By comparing with the result of Fig. 10(e), the former is identified as the true mass solution, while the latter is a spurious solution. The spurious solution arises from the nonlinearity of the mode shape functions [82, 83]. Based on the results presented in Fig. 10, a strategy to eliminate spurious solutions and obtain the true one can be summarized: Since in flow-through detection the particle position changes over time, multiple identification results obtained at different positions can be used to identify the true solution.



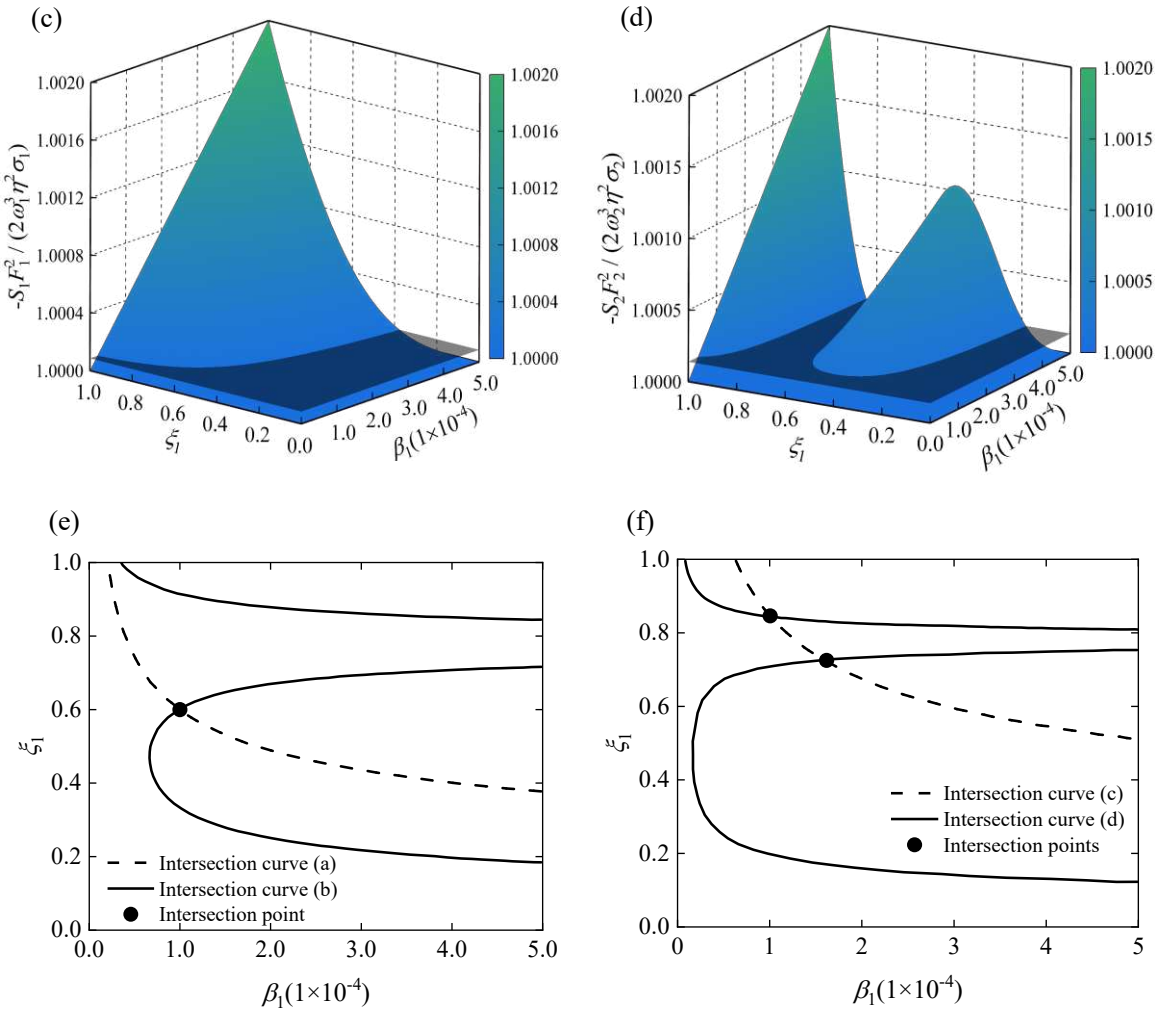
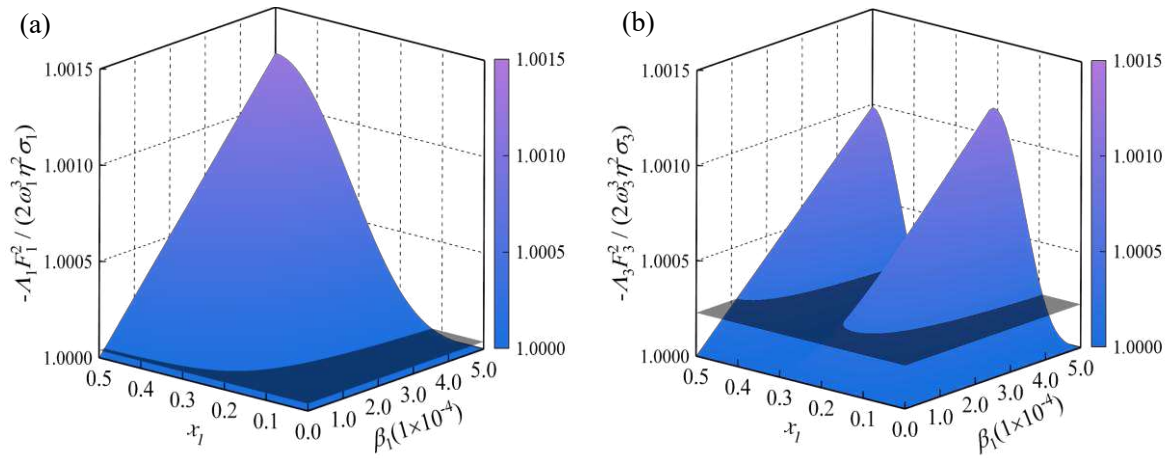


Fig. 10 Identification process for a single particle ($\beta_1 = 1.00\times10^{-4}$) at different positions in the cantilevered SMR ($L = 10b$, $\mu = 0.1$, $V_{DC} = 1$, $V_{AC} = 0.4$, $Q = 200$). For the particle located at $\xi_1 = 0.6$: (a) identification result based on the peak frequency shift of the first mode; (b) identification result based on the peak frequency shift of the second mode. For the particle located at $\xi_1 = 0.85$: (c) identification result based on the peak frequency shift of the first mode; (d) identification result based on the peak frequency shift of the second mode. (e) Projection of the intersecting curves shown in (a) and (b). (f) Projection of the intersecting curves shown in (c) and (d).



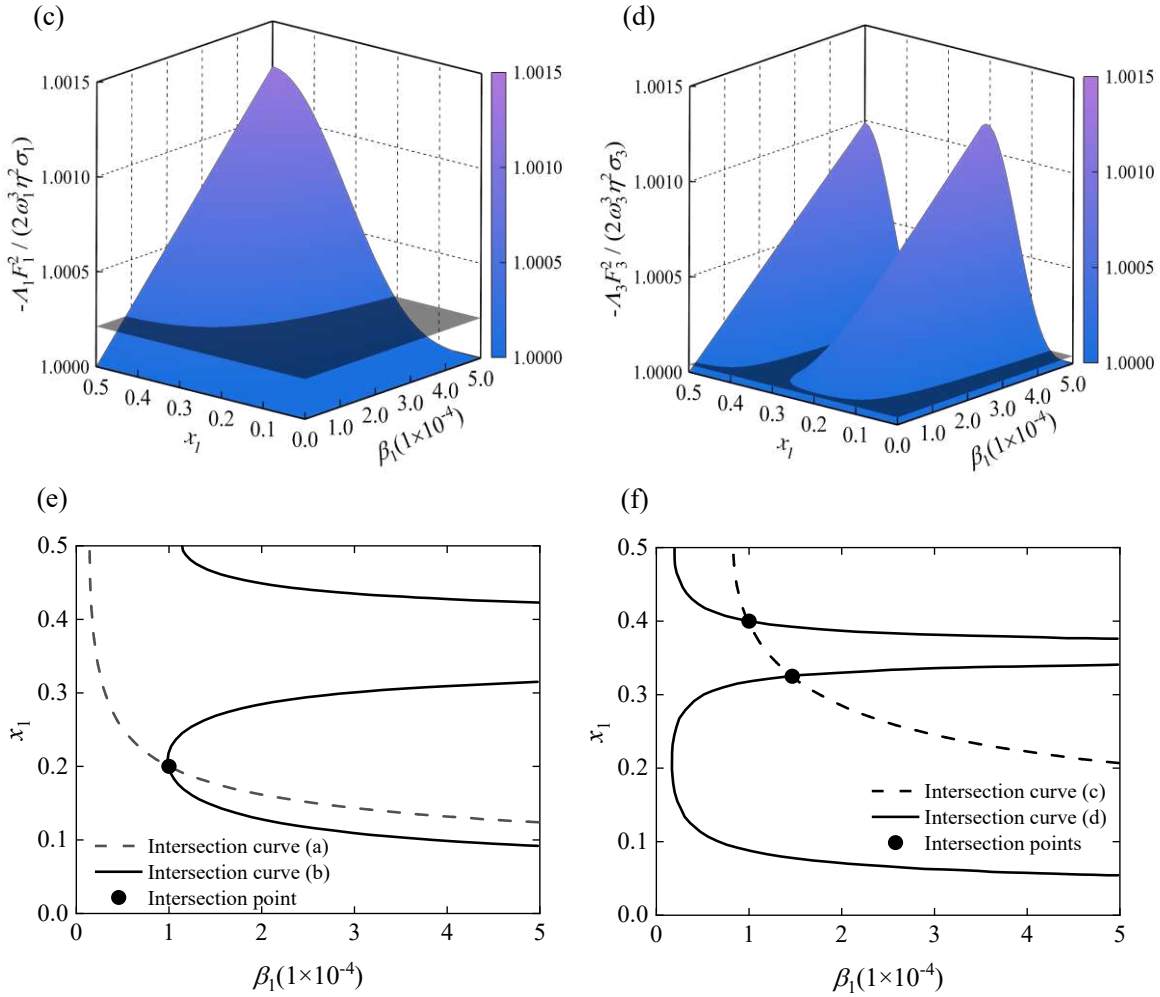


Fig. 11 Identification process for a single particle (β_1 = 1.00×10^{-4}) at different positions in the doubly clamped SMR (L = 20b, μ = 0.1, N_F = 0, V_{DC} = 1, V_{AC} = 0.4, Q = 200). For the particle located at x_1 = 0.2: (a) identification result based on the peak frequency shift of the first mode; (b) identification result based on the peak frequency shift of the third mode. For the particle located at ξ_1 = 0.4: (c) identification result based on the peak frequency shift of the first mode; (d) identification result based on the peak frequency shift of the third mode. (e) Projection of the intersecting curves shown in (a) and (b). (f) Projection of the intersecting curves shown in (c) and (d).

The identification of a single particle (β_1 = 1.00×10^{-4}) in the doubly clamped SMR is shown in Fig. 11. For a particle located at x_1 = 0.200, the detection results based on the peak frequency shifts of the first two symmetric modes are presented in Figs. 11(a) and (b), respectively. In these figures, the curved surfaces represent the left-hand side of Eq. (49) as a function of the mass β_1 and position x_1, while the planes correspond to the right-hand side of Eq. (49) evaluated with the peak frequency calculated from Eq. (47). The intersecting curves from Figs. 11(a) and (b) are

projected onto the β_1-x_1 plane, resulting in Fig. 11(e). The intersection point of the projected curves in Fig. 11(e) is ($\beta_1 = 1.00\times10^{-4}$, $x_1 = 0.200$), which is the identification result obtained by using the peak frequency shifts of the first two symmetric modes based on Eq. (49). For the particle located at $x_1 = 0.400$, the detection results based on the first two symmetric modes are shown in Figs. 11(c) and (d), respectively. Two intersection points are observed in Fig. 11(f): ($\beta_1 = 1.00\times10^{-4}$, $x_1 = 0.400$) and ($\beta_1 = 1.47\times10^{-4}$, $x_1 = 0.325$). By comparing with the result in Fig. 11(e), it can be determined that ($\beta_1 = 1.00\times10^{-4}$, $x_1 = 0.400$) is the true solution, while the other is a spurious solution.

The mass detection of two particles at different positions inside a cantilevered SMR is presented in Table 1. Since both the masses and positions of the two particles are unknown, the peak frequencies of the first four modes are required. For the case where the true masses and positions are ($\beta_1 = 1.00\times10^{-3}$, $\xi_1 = 0.150$) and ($\beta_2 = 3.00\times10^{-3}$, $\xi_2 = 0.500$), it is assumed that the peak frequencies calculated from Eq. (39) are consistent with the experimental measurements. These peak frequencies are then substituted into Eq. (48) to retrieve the masses and positions of the particles. As can be seen from Table 1, only one set of results is obtained in this case, namely ($\beta_1 = 1.00\times10^{-3}$, $\xi_1 = 0.150$) and ($\beta_2 = 3.00\times10^{-3}$, $\xi_2 = 0.500$), which agrees with the true values. When the particle positions are changed to $\xi_1 = 0.600$ and $\xi_2 = 0.900$, in addition to the true result, one spurious solution is obtained: ($\beta_1 = 0.92\times10^{-3}$, $\xi_1 = 0.388$) and ($\beta_2 = 3.33\times10^{-3}$, $\xi_2 = 0.890$). For the positions $\xi_1 = 0.750$ and $\xi_2 = 0.980$, two spurious solutions are obtained. By comparing the identification results obtained for different particle positions, it is found that the true mass solution remains unique and invariant across all sets of results. Accordingly, the spurious solutions can be eliminated, and the true masses of the particles to be detected are determined to be $\beta_1 = 1.00\times10^{-3}$ and $\beta_2 = 3.00\times10^{-3}$. Furthermore, the identification results for two particles with masses $\beta_1 = 2.50\times10^{-3}$ and $\beta_2 = 5.30\times10^{-3}$ at various positions are also given in Table 1. Similarly, the true solution is present in each set of results and remains unique across different positions. Thus, the spurious solutions can be

excluded and the final true result is obtained.

Table 1 Detection of two particles in the cantilevered SMR ($L = 10b$, $\mu = 0.1$, $V_{DC} = 1$, $V_{AC} = 0.4$, $Q = 200$).

Exact mass ($\beta_1\times10^{-3}$, $\beta_2\times10^{-3}$)	Exact position (ξ_1, ξ_2)	Result 1 ($\beta_1\times10^{-3}$, ξ_1) ($\beta_2\times10^{-3}$, ξ_2)	Result 2 ($\beta_1\times10^{-3}$, ξ_1) ($\beta_2\times10^{-3}$, ξ_2)	Result 3 ($\beta_1\times10^{-3}$, ξ_1) ($\beta_2\times10^{-3}$, ξ_2)	True result ($\beta_1\times10^{-3}$, $\beta_2\times10^{-3}$)
(1.00, 3.00)	(0.150, 0.500)	(1.00, 0.150) (3.00, 0.500)	/	/	(1.00, 3.00)
	(0.600, 0.900)	(1.00, 0.600) (3.00, 0.900)	(0.92, 0.388) (3.33, 0.890)	/	
	(0.750, 0.980)	(1.00, 0.750) (3.00, 0.980)	(2.51, 0.216) (3.75, 0.950)	(3.48, 0.782) (7.24, 0.603)	
(2.50, 5.30)	(0.100, 0.200)	(2.50, 0.10) (5.30, 0.20)	/	/	(2.50, 5.30)
	(0.350, 0.400)	(2.50, 0.350) (5.30, 0.400)	/	/	
	(0.900, 0.700)	(2.50, 0.900) (5.30, 0.700)	(3.14, 0.850) (5.66, 0.671)	/	

Mass detection of two particles at different positions inside the doubly clamped SMR is presented in Table 2. The peak frequencies of the first four symmetric modes are used for detection. For two particles with masses $\beta_1 = 1.20\times10^{-3}$ and $\beta_2 = 3.50\times10^{-3}$, two identification results are obtained at each of the three different positions. The true mass solution remains unchanged across all results, while the others are spurious. Due to the structural symmetry of the doubly clamped beam, the identified particle positions are confined to the range $x \in [0, 0.5]$. Consequently, when the particle with mass $\beta_1 = 1.20\times10^{-3}$ is actually located at $x_1 = 0.800$, the method yields a position of $x_1 = 0.200$. Nevertheless, the accuracy of the determined masses is not affected. In the particle identification process, mass information plays a more important role than position information [84, 85]. Identification results for two particles with masses $\beta_1 = 0.95\times10^{-3}$ and $\beta_2 = 0.84\times10^{-3}$ are also given in Table 2. Again, although multiple identification results are obtained for different particle positions, the true solution remains the only invariant across all sets.

Table 2 Detection of two particles in the clamped-clamped beam SMR ($L = 20b$, $\mu = 0.1$, $N_F = 0$, $V_{DC} = 1$, $V_{AC} = 0.4$, $Q = 200$).

Exact mass ($\beta_1\times10^{-3}$, $\beta_2\times10^{-3}$)	Exact position (x_1, x_2)	Result 1 ($\beta_1\times10^{-3}$, x_1) ($\beta_2\times10^{-3}$, x_2)	Result 2 ($\beta_1\times10^{-3}$, x_1) ($\beta_2\times10^{-3}$, x_2)	Result 3 ($\beta_1\times10^{-3}$, x_1) ($\beta_2\times10^{-3}$, x_2)	True result ($\beta_1\times10^{-3}$, $\beta_2\times10^{-3}$)
(1.20, 3.50)	(0.150, 0.250)	(1.20, 0.150) (3.50, 0.250)	(4.24, 0.067) (3.94, 0.244)	/	(1.20, 3.50)
	(0.450, 0.320)	(1.20, 0.450) (3.50, 0.320)	(1.72, 0.372) (3.77, 0.300)	/	
	(0.800, 0.400)	(1.20, 0.200) (3.50, 0.400)	(1.48, 0.257) (3.10, 0.405)	/	
(0.95, 0.84)	(0.100, 0.200)	(0.95, 0.100) (0.84, 0.200)	(0.88, 0.107) (0.81, 0.201)	/	(0.95, 0.84)
	(0.200, 0.350)	(0.95, 0.200) (0.84, 0.350)	(1.00, 0.245) (0.75, 0.324)	(0.45, 0.179) (0.66, 0.476)	
	(0.400, 0.900)	(0.95, 0.400) (0.84, 0.100)	(0.51, 0.340) (0.50, 0.462)	(0.77, 0.363) (0.66, 0.276)	

During the operation of the resonator, noise is inevitably introduced [86, 87]. To evaluate the effect of noise on particle mass detection and the robustness of the proposed identification method, the particle mass under noise interference is expressed as follows [7, 82]:

$$\beta_p = \beta_p^{\text{exact}} + \beta_p^{\text{noise}}, \tag{50}$$

where β_p^{exact} is the exact mass of the particle, and β_p^{noise} represents the contribution due to noise. By considering the effect of Gaussian noise on the frequency measurement, the following expression is obtained from Eq. (48) for the cantilevered SMR [7, 82]:

$$\begin{cases} 1+\beta_1\phi_1^2(\xi_1)+\beta_2\phi_1^2(\xi_2)+\cdots+\beta_p\phi_1^2(\xi_p) = -\dfrac{S_1F_1^2}{2\omega_1^3\eta^2\left[\sigma_1+\chi^{\text{noise}}r_g(1+\sigma_1)\right]}, \\ 1+\beta_1\phi_2^2(\xi_1)+\beta_2\phi_2^2(\xi_2)+\cdots+\beta_p\phi_2^2(\xi_p) = -\dfrac{S_2F_2^2}{2\omega_2^3\eta^2\left[\sigma_2+\chi^{\text{noise}}r_g(1+\sigma_2)\right]}, \\ \vdots \\ 1+\beta_1\phi_p^2(\xi_1)+\beta_2\phi_p^2(\xi_2)+\cdots+\beta_p\phi_p^2(\xi_p) = -\dfrac{S_pF_p^2}{2\omega_p^3\eta^2\left[\sigma_p+\chi^{\text{noise}}r_g(1+\sigma_p)\right]}. \end{cases} \tag{51}$$

where χ^{noise} is the uncertainty of the Gaussian noise, with larger values indicating a higher noise level, and r_{g} is a random number following the standard normal distribution. Similarly, the following expression is obtained for the doubly clamped SMR based on Eq. (49):

$$\begin{cases} 1+\beta_1\varphi_1^2\left(x_1\right)+\beta_2\varphi_1^2\left(x_2\right)+\cdots+\beta_p\varphi_1^2\left(x_p\right)=-\dfrac{\Lambda_1 F_1^2}{2\omega_1^3\eta^2\left[\sigma_1+\chi^{\text{noise}}r_g\left(1+\sigma_1\right)\right]}, \\ 1+\beta_1\varphi_2^2\left(x_1\right)+\beta_2\varphi_2^2\left(x_2\right)+\cdots+\beta_p\varphi_2^2\left(x_p\right)=-\dfrac{\Lambda_2 F_2^2}{2\omega_2^3\eta^2\left[\sigma_2+\chi^{\text{noise}}r_g\left(1+\sigma_2\right)\right]}, \\ \vdots \\ 1+\beta_1\varphi_p^2\left(x_1\right)+\beta_2\varphi_p^2\left(x_2\right)+\cdots+\beta_p\varphi_p^2\left(x_p\right)=-\dfrac{\Lambda_p F_p^2}{2\omega_p^3\eta^2\left[\sigma_p+\chi^{\text{noise}}r_g\left(1+\sigma_p\right)\right]}. \end{cases} \tag{52}$$

To eliminate possible spurious solutions, the particle positions in Eqs. (51) and (52) are taken as known exact values, while the particle masses are unknown and to be determined [7, 82].

The relative probability density (RPD) of the particle mass deviation $\beta_1^{\text{noise}}/\beta_1^{\text{exact}}$ during the mass detection of a single particle is shown in Figs. 12(a) and 12(b) for the cantilever and doubly clamped SMRs, respectively. For single-particle mass detection, only the peak frequency of the first mode is required under the assumption that the particle position is exactly known. For each noise uncertainty χ^{noise}, 100,000 random samples r_{g} are generated. These samples are then substituted into Eqs. (51) and (52) to calculate the probability density P_χ of the particle mass deviation. The maximum of the probability density is denoted as $P_\chi^{\max}$, and the RPD is obtained by $P_\chi/P_\chi^{\max}$. As shown in Fig. 12(a), for a noise uncertainty of $\chi^{\text{noise}} = 1\times10^{-6}$, the probability that the particle mass deviation is within 5% is 66.52%. When the noise uncertainty is reduced to $\chi^{\text{noise}} = 1\times10^{-7}$, this probability increases to 100%. Therefore, the accuracy of particle mass detection is improved when noise is suppressed. In Fig. 12(b), for a noise uncertainty of $\chi^{\text{noise}} = 1\times10^{-4}$, the probability of the mass deviation being within 5% is 37.21%. When the noise uncertainty is decreased to $\chi^{\text{noise}} = 1\times10^{-5}$, the probability reaches 100%. Similar to Fig. 12(a), it is concluded that the particle mass deviation decreases as the noise uncertainty is

lowered.

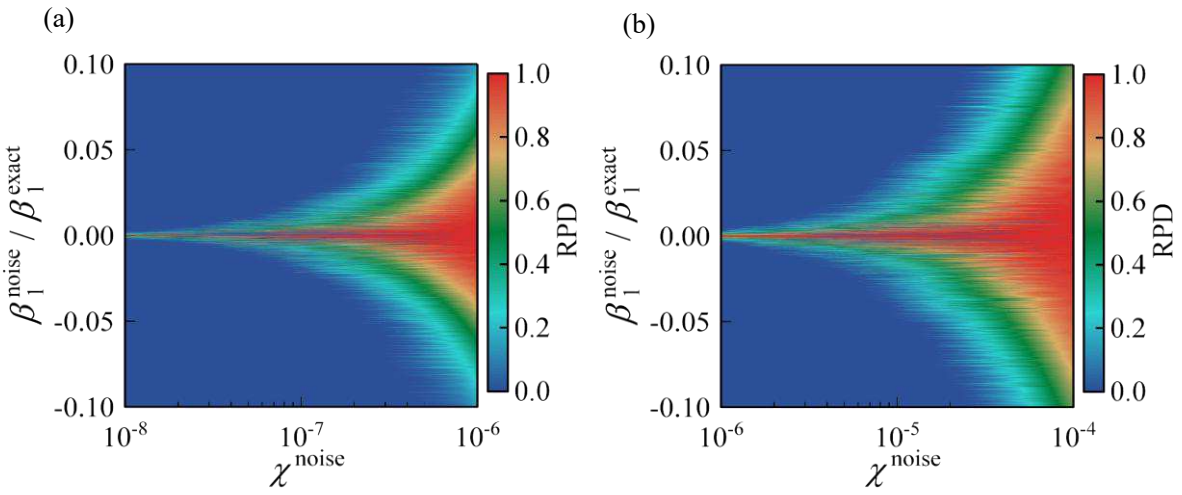


Fig. 12 The relative probability density (RPD) of the $\beta_1^{noise}/\beta_1^{exact}$ as a function of the noise uncertainty χ^{noise}. (a) The RPD for a single particle (β_1^{exact} = 1.00×10^{-3}, ξ_1 = 0.700) in the cantilevered SMR (L = 10b, μ = 0.1, V_{DC} = 1, V_{AC} = 0.4, Q = 200). (b) The RPD for a single particle (β_1^{exact} = 1.00×10^{-3}, x_1 = 0.400) in the clamped-clamped beam SMR (L = 20b, μ = 0.1, N_F = 0, V_{DC} = 1, V_{AC} = 0.4, Q = 200).

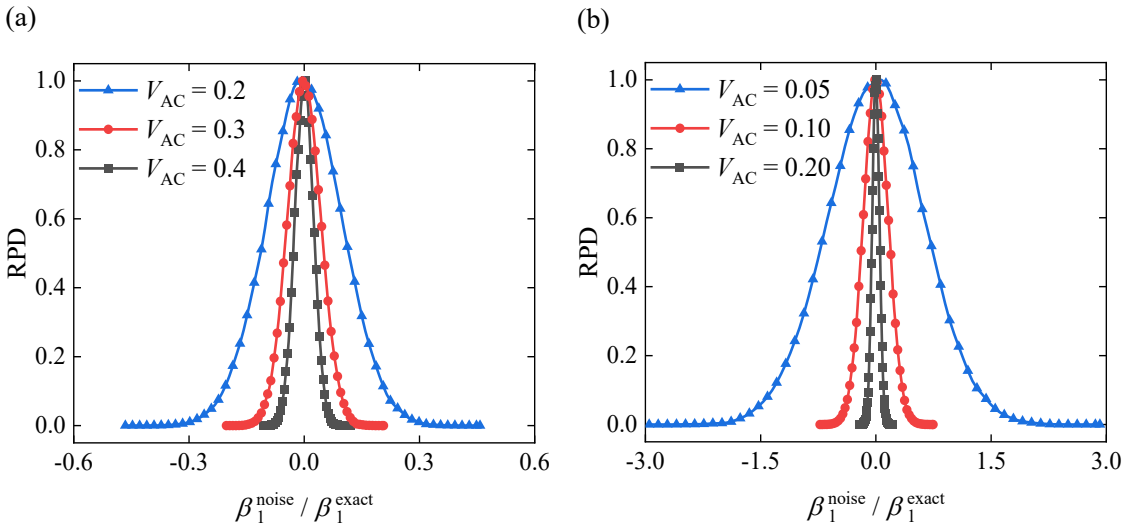


Fig. 13 The influence of the actuation voltage V_{AC} on the RPD of the particle mass deviation $\beta_1^{noise}/\beta_1^{exact}$. (a) The RPD for a single particle (β_1^{exact} = 1.00×10^{-3}, ξ_1 = 0.900) in the cantilevered SMR (L = 10b, μ = 0.1, V_{DC} = 1, Q = 200, χ^{noise} = 1×10^{-6}). (b) The RPD for a single particle (β_1^{exact} = 1.00×10^{-3}, x_1 = 0.300) in the clamped-clamped beam SMR (L = 20b, μ = 0.1, N_F = 0, V_{DC} = 1, Q = 200, χ^{noise} = 1×10^{-5}).

The effects of the driving voltage V_{AC} on the RPD of the particle mass deviation are shown in Figs. 13(a) and 13(b) for the cantilever and doubly clamped SMRs,

respectively. For single-particle mass detection, the peak frequency of the first mode is used. In Fig. 13(a), as V_{AC} increases from 0.2 to 0.4, the RPD curve becomes narrower, indicating that the error in the detected particle mass is reduced under noise. Moreover, it can be observed from Fig. 5(a) that when V_{AC} is increased to 0.4, the amplitude-frequency response curve exhibits a pronounced softening effect. This indicates that a resonator driven in the nonlinear regime possesses a higher noise immunity than that driven in the linear regime. A similar narrowing of the RPD curve is also observed in Fig. 13(b). These results suggest that increasing the driving voltage mitigates noise interference in mass detection for both the cantilever and doubly clamped SMRs.

3.3 Validation of the results

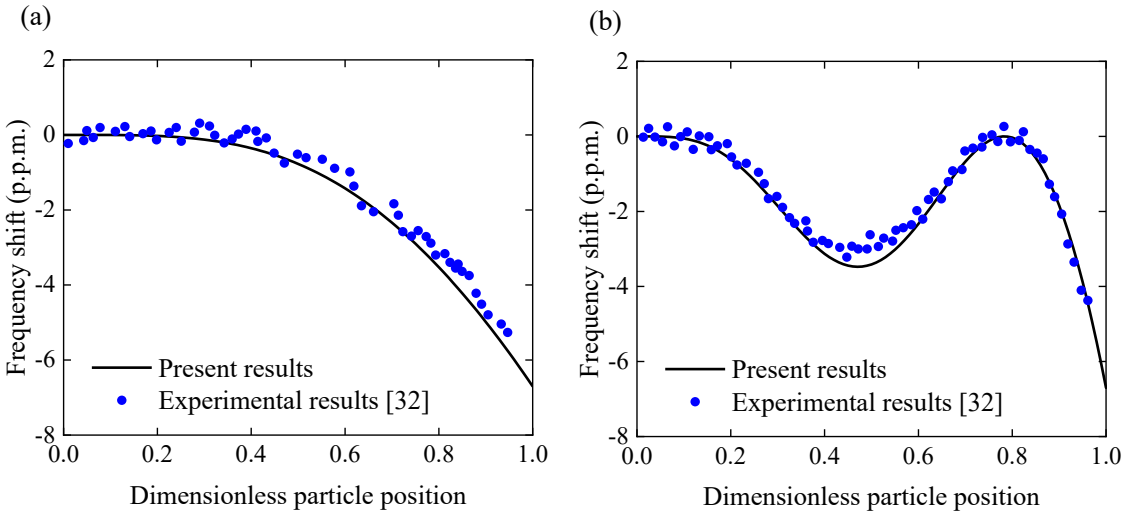


Fig. 14 The comparison of the resonance frequency shifts induced by a 100 nm gold particle in a cantilevered SMR with experimental results [32]: (a) first-mode resonance frequency shift; (b) second-mode resonance frequency shift.

To validate the theoretical results, comparisons between the theoretically predicted and experimentally measured resonance frequency shifts of the first two modes of the cantilevered SMR, induced by a 100 nm gold particle, are presented in Figs. 14(a) and 14(b), respectively. The cantilevered SMR is with the length, width, and thickness of

200 μm, 16 μm, and 1.3 μm, respectively, while the internal fluid channel has a width of 2 μm and a height of 700 nm [32]. The results shown in Fig. 14 demonstrate good agreement between the present theoretical predictions and the experimental measurements, with only small deviations. The minor discrepancies can be attributed to the difference between the actual geometric dimensions of the SMR and its nominal design specifications [28, 32].

A reduced-order model is developed based on the Galerkin method to validate the nonlinear amplitude-frequency response of the SMR. The deflection of the cantilevered SMR is written as:

$$w(\xi,\ t) = w_s(\xi) + w_d(\xi, t) = w_s(\xi) + \sum_{i=1}^{N} \phi_i(\xi) q_i(t), \tag{53}$$

where $q_i(t)$ is time-dependent generalized coordinate. Equation (53) is substituted into the governing equation (10), and only the time-dependent terms are retained. Both sides of the resulting equation are then multiplied by ϕ_j and integrated over $\xi \in [0,\ 1]$, yielding:

$$\sum_{i=1}^{N} M_{ij}\ddot{q}_i + \sum_{i=1}^{N} C_{ij}\dot{q}_i + \sum_{i=1}^{N} K_{ij} q_i + \sum_{i=1}^{N}\sum_{k=1}^{N} K_{ijk} q_i q_k + \sum_{i=1}^{N}\sum_{k=1}^{N}\sum_{l=1}^{N} K_{ijkl} q_i q_k q_l = F_j \cos(\Omega t). \tag{54}$$

The expressions for the coefficients in Eq. (54) are given in Appendix B. Four modes are employed to solve Eq. (54) numerically by using the Runge-Kutta method [40, 57]. A reduced-order model for the doubly clamped SMR is obtained by following a similar derivation procedure, which takes the same form as Eq. (54) except for the coefficients. The specific expressions of these coefficients are also provided in Appendix B.

A comparison between the amplitude-frequency response of the first mode of the cantilevered SMR obtained by the perturbation method and that obtained by the Runge-Kutta method is shown in Fig. 15(a). Good agreement is observed between the theoretical and numerical results. In Fig. 15(b), the time history at σ = 0 is presented, which is a stable periodic solution. This is consistent with the stable solution corresponding to $\sigma = 0$ in Fig. 15(a). The comparison for the first mode of the doubly clamped SMR is shown in Fig. 15(c), and its time history at σ = 0 is presented in Fig.

15(d). Again, good agreement is observed between the theoretical and numerical results.

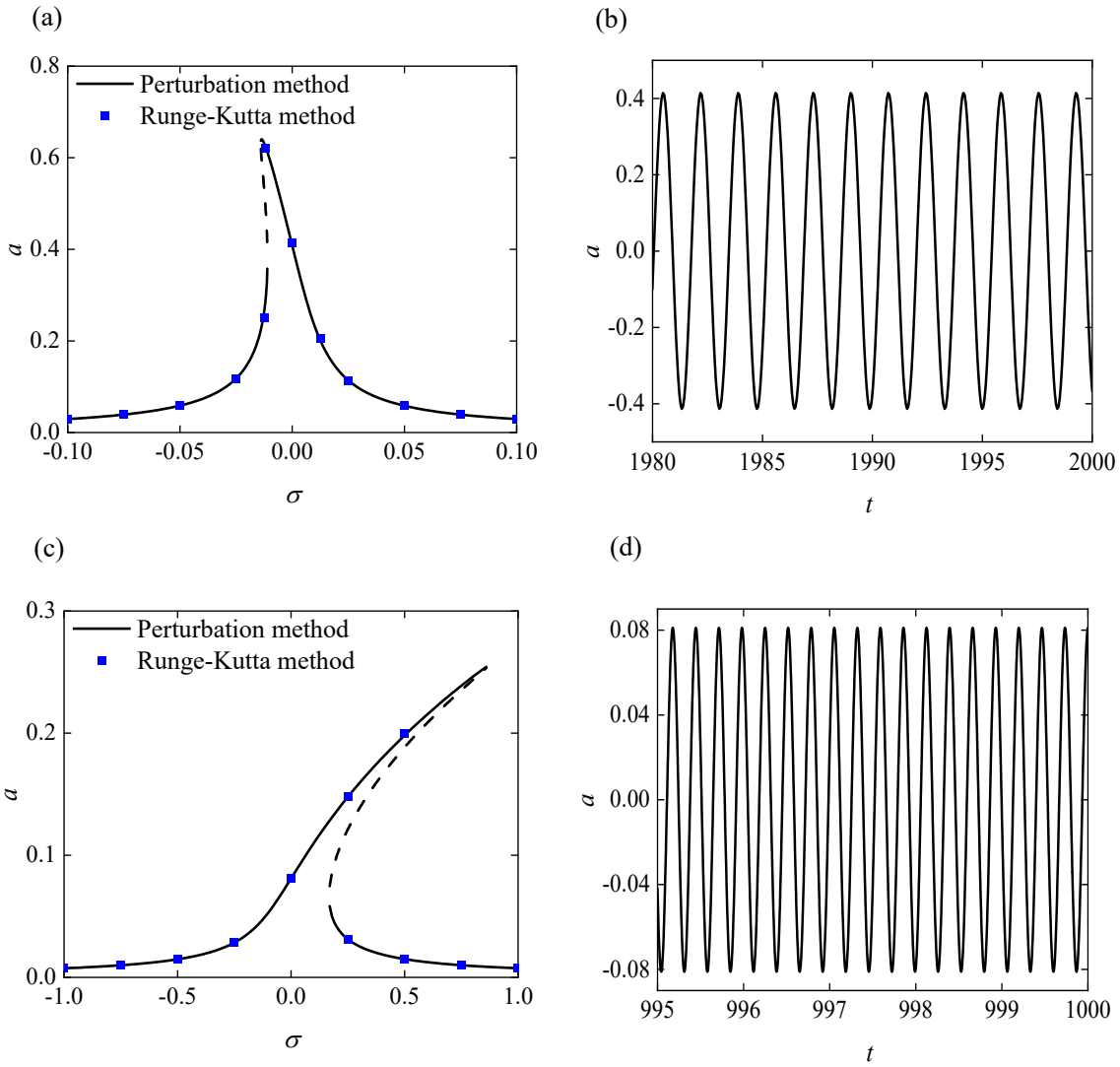


Fig. 15 Validation of the nonlinear response. For the cantilevered SMR ($L = 10b$, $\mu = 0.1$, $V_{DC} = 1$, $Q = 200$): (a) comparison between the amplitude-frequency response of the first mode obtained by the perturbation method and that from the Runge-Kutta method at $V_{AC} = 0.4$; (b) time history at $\sigma = 0$. For the doubly clamped SMR ($L = 20b$, $\mu = 0.1$, $N_F = 0$, $V_{DC} = 1$, $Q = 200$): (c) comparison between the amplitude-frequency response of the first mode obtained by the perturbation method and that from the Runge-Kutta method at $V_{AC} = 0.4$; (d) time history at $\sigma = 0$.

4 Conclusions

In this work, a theoretical model of the SMRs with multiple suspended particles is established by incorporating both geometric and electrostatic nonlinearities.

Approximate analytical solutions for the dynamic responses of cantilever and doubly clamped SMRs are obtained by using the method of multiple scales. The results show that at a relatively high driving voltage, the dynamic responses of the SMRs tends to be dominated by the softening effect of the electrostatic force. Consequently, the resonance frequencies decrease and the amplitude-frequency response curves bend to the left. As the order of the vibration mode increases, the hardening effect of geometric nonlinearity becomes stronger. In this case, the decrease in resonance frequencies is counteracted, or the frequencies even increase, and the amplitude-frequency response curves bend to the right.

Furthermore, a method for detecting multiple suspended particles is developed based on shifts of the nonlinear peak frequencies. The procedures for identifying a single particle and two particles by using the proposed method are presented through numerical examples. It is shown that the present method yields the masses of particles at arbitrary positions in the suspended microchannel. Spurious solutions in the identification results are eliminated by the existence and uniqueness of the true particle mass solution. The robustness of the proposed method under noise interference is verified by considering the effect of Gaussian noise on mass detection. Moreover, SMRs driven in the nonlinear regime exhibit good noise immunity.

Author contributions Y. Z designed the research, J. W carried out the derivation and computation; J. W and Y. Z wrote the manuscript.

Funding This work was supported by Chinese Academy of Sciences (Grant Nos. E6XS040254).

Data availability No data was used for the research described in the article.

Declarations

Conflicts of interest The authors declare no competing interests.

Appendix A

The solution to Eqs. (42) and (43) is assumed as:

$$w(x,\ t;\ \varepsilon) = w_s(x) + w_d(x,t;\varepsilon) = w_s(x) + \sum_{i=1}^{3} \varepsilon^i w_i\left(x, T_0, T_2\right). \tag{A1}$$

Then, the following expressions are derived by substituting (A1) into Eqs. (42) and (43):

Order ε^0:

$$(1+\mu)\frac{\partial^4 w_s}{\partial x^4} - \left[N_F + \alpha_3 \int_0^1 \left(\frac{\partial w_s}{\partial x}\right)^2 dx\right]\frac{\partial^2 w_s}{\partial x^2} = \frac{\alpha_2 V_{\mathrm{DC}}^2}{(1-w_s)^2}. \tag{A2}$$

The static deflection component is governed by Eq. (A2), and the corresponding boundary conditions are:

$$w_s\big|_{x=0} = 0,\ \left.\frac{\partial w_s}{\partial x}\right|_{x=0} = 0,\ w_s\big|_{x=1} = 0,\ \left.\frac{\partial w_s}{\partial x}\right|_{x=1} = 0. \tag{A3}$$

Order ε^1:

$$\Gamma(w_1) = 0, \tag{A4}$$

where

$$\begin{aligned}\Gamma(w_i) = &\left[1 + \sum_{p=1}^{P} \beta_p \delta_D(x - x_p)\right] D_0^2 w_i + (1+\mu)\frac{\partial^4 w_i}{\partial x^4} - \left[N_F + \alpha_3 \int_0^1 \left(\frac{\partial w_s}{\partial x}\right)^2 dx\right]\frac{\partial^2 w_i}{\partial x^2} \\ &-2\alpha_3 \frac{\partial^2 w_s}{\partial x^2}\int_0^1 \frac{\partial w_s}{\partial x}\frac{\partial w_i}{\partial x}dx - \frac{2\alpha_2 V_{\mathrm{DC}}^2}{(1-w_s)^3} w_i.\end{aligned} \tag{A5}$$

Order ε^2:

$$\Gamma(w_2) = \alpha_3 \frac{\partial^2 w_s}{\partial x^2}\int_0^1 \left(\frac{\partial w_1}{\partial x}\right)^2 dx + 2\alpha_3 \frac{\partial^2 w_1}{\partial x^2}\int_0^1 \frac{\partial w_s}{\partial x}\frac{\partial w_1}{\partial x}dx + \frac{3\alpha_2 V_{\mathrm{DC}}^2}{(1-w_s)^4} w_1^2. \tag{A6}$$

Order ε^3:

$$\Gamma\left(w_3\right)=-2\left[1+\sum_{p=1}^{P}\beta_p\delta_D(x-x_p)\right]D_0D_2w_1-cD_0w_1+2\alpha_3\frac{\partial^2 w_s}{\partial x^2}\int_0^1\frac{\partial w_1}{\partial x}\frac{\partial w_2}{\partial x}dx$$
$$+2\alpha_3\frac{\partial^2 w_1}{\partial x^2}\int_0^1\frac{\partial w_s}{\partial x}\frac{\partial w_2}{\partial x}dx+2\alpha_3\frac{\partial^2 w_2}{\partial x^2}\int_0^1\frac{\partial w_s}{\partial x}\frac{\partial w_1}{\partial x}dx+\frac{4\alpha_2V_{\mathrm{DC}}^2}{\left(1-w_s\right)^5}w_1^3 \tag{A7}$$
$$+\alpha_3\frac{\partial^2 w_1}{\partial x^2}\int_0^1\left(\frac{\partial w_1}{\partial x}\right)^2dx+\frac{6\alpha_2V_{\mathrm{DC}}^2}{\left(1-w_s\right)^4}w_1w_2+\frac{2\alpha_2V_{\mathrm{DC}}V_{\mathrm{AC}}\cos\left(\Omega t\right)}{\left(1-w_s\right)^2}.$$

The boundary conditions for Eqs. (A4), (A6) and (A7) are:

$$w_i\big|_{x=0}=0,\ \left.\frac{\partial w_i}{\partial x}\right|_{x=0}=0,\ w_i\big|_{x=1}=0,\ \left.\frac{\partial w_i}{\partial x}\right|_{x=1}=0. \tag{A8}$$

The solution to Eqs. (A4) and (A8) is:

$$w_1\left(x,T_0,T_2\right)=\varphi\left(x\right)A\left(T_2\right)\mathrm{e}^{i\omega T_0}+\varphi\left(x\right)\overline{A}\left(T_2\right)\mathrm{e}^{-i\omega T_0}, \tag{A9}$$

where ω and φ are the frequency and mode shape of the clamped-clamped beam. The substitution of Eq. (A9) into Eq. (A6) yields:

$$\Gamma\left(w_2\right)=\left(A^2\mathrm{e}^{2i\omega T_0}+2A\overline{A}+\overline{A}^2\mathrm{e}^{-2i\omega T_0}\right)H\left(x\right), \tag{A10}$$

where

$$H\left(x\right)=\alpha_3\frac{\partial^2 w_s}{\partial x^2}\int_0^1\left(\frac{\partial\varphi}{\partial x}\right)^2dx+2\alpha_3\frac{\partial^2\varphi}{\partial x^2}\int_0^1\frac{\partial w_s}{\partial x}\frac{\partial\varphi}{\partial x}dx+\frac{3\alpha_2V_{\mathrm{DC}}^2}{\left(1-w_s\right)^4}\varphi^2. \tag{A11}$$

A particular solution to Eqs. (A10) and (A8) is given by:

$$w_2\left(x,T_0,T_2\right)=\psi_3\left(x\right)A^2\left(T_2\right)\mathrm{e}^{2i\omega T_0}+2\psi_4\left(x\right)A\overline{A}+\psi_3\left(x\right)\overline{A}^2\mathrm{e}^{-2i\omega T_0}, \tag{A12}$$

where ψ_3 and ψ_4 are solutions to:

$$H\left(x\right)=-4\omega^2\psi_3\left[1+\sum_{p=1}^{P}\beta_p\delta_D(x-x_p)\right]-\left[N_F+\alpha_3\int_0^1\left(\frac{\partial w_s}{\partial x}\right)^2dx\right]\frac{\partial^2\psi_3}{\partial x^2}$$
$$+\left(1+\mu\right)\psi_3''''-2\alpha_3\frac{\partial^2 w_s}{\partial x^2}\int_0^1\frac{\partial w_s}{\partial x}\frac{\partial\psi_3}{\partial x}dx-\frac{2\alpha_4V_{\mathrm{DC}}^2}{\left(1-w_s\right)^3}\psi_3, \tag{A13}$$

$$H\left(x\right)=\left(1+\mu\right)\psi_4''''-2\alpha_3\frac{\partial^2 w_s}{\partial x^2}\int_0^1\frac{\partial w_s}{\partial x}\frac{\partial\psi_4}{\partial x}dx-\frac{2\alpha_4V_{\mathrm{DC}}^2}{\left(1-w_s\right)^3}\psi_4$$
$$-\left[N_F+\alpha_3\int_0^1\left(\frac{\partial w_s}{\partial x}\right)^2dx\right]\frac{\partial^2\psi_4}{\partial x^2}, \tag{A14}$$

$$\psi_j\big|_{x=0}=0,\ \left.\frac{\partial\psi_j}{\partial x}\right|_{x=0}=0,\ \psi_j\big|_{x=1}=0,\ \left.\frac{\partial\psi_j}{\partial x}\right|_{x=1}=0,\ j=3,4. \tag{A15}$$

The following expressions are obtained by substituting Eqs. (28), (A9), and (A12) into Eq. (A7):

$$\begin{aligned}\Gamma\left(w_3\right)=&-2i\omega\frac{\partial A}{\partial T_2}\left[1+\sum_{p=1}^{P}\beta_p\delta_D(x-x_p)\right]\varphi\mathrm{e}^{i\omega T_0}-i\omega cA\varphi\mathrm{e}^{i\omega T_0}\\&+\left[X\left(x\right)A^2\overline{A}+\chi_F\left(x\right)\mathrm{e}^{i\sigma T_2}\right]\mathrm{e}^{i\omega T_0}+\mathrm{cc}+\mathrm{NST},\end{aligned}\tag{A16}$$

$$X\left(x\right)=X_q^G\left(x\right)+X_c^G\left(x\right)+X_q^E\left(x\right)+X_c^E\left(x\right),\tag{A17}$$

$$\begin{aligned}X_q^G\left(\xi\right)=&\left(2\alpha_3\frac{\partial^2\psi_3}{\partial x^2}+4\alpha_3\frac{\partial^2\psi_4}{\partial x^2}\right)\int_0^1\frac{\partial w_s}{\partial x}\frac{\partial\varphi}{\partial x}dx+2\alpha_3\frac{\partial^2 w_s}{\partial x^2}\int_0^1\frac{\partial\varphi}{\partial x}\frac{\partial\psi_3}{\partial x}dx\\&+4\alpha_3\frac{\partial^2 w_s}{\partial x^2}\int_0^1\frac{\partial\varphi}{\partial x}\frac{\partial\psi_4}{\partial x}dx+2\alpha_3\frac{\partial^2\varphi}{\partial x^2}\int_0^1\frac{\partial w_s}{\partial x}\frac{\partial\psi_3}{\partial x}dx\\&+4\alpha_3\frac{\partial^2\varphi}{\partial x^2}\int_0^1\frac{\partial w_s}{\partial x}\frac{\partial\psi_4}{\partial x}dx,\end{aligned}\tag{A18}$$

$$X_c^G\left(x\right)=3\alpha_3\frac{\partial^2\varphi}{\partial x^2}\int_0^1\left(\frac{\partial\varphi}{\partial x}\right)^2dx,\tag{A19}$$

$$X_q^E\left(\xi\right)=\frac{6\alpha_2V_{\mathrm{DC}}^2}{\left(1-w_s\right)^4}\left(2\varphi\psi_4+\varphi\psi_3\right),\ X_c^E\left(\xi\right)=\frac{4\alpha_2V_{\mathrm{DC}}^2}{\left(1-w_s\right)^5}\varphi^3.\tag{A20}$$

In Eq. (A17), the quadratic and cubic terms from geometric nonlinearity are X_q^G and X_c^G, and those from electrostatic nonlinearity are X_q^E and X_c^E. To derive the solvability condition, the right-hand side of Eq. (A16) is multiplied by $\varphi\mathrm{e}^{-i\omega T_0}$ and then integrated over $x\in[0,\ 1]$:

$$2i\omega\frac{\partial A}{\partial T_2}\left[1+\sum_{p=1}^{P}\beta_p\varphi^2\left(x_p\right)\right]+i\omega\eta A-\Lambda A^2\overline{A}-F\mathrm{e}^{i\sigma T_2}=0,\tag{A21}$$

where

$$\Lambda=\int_0^1 X\varphi d\xi.\tag{A22}$$

By writing A in polar form as $A=\left(1/2\right)a\mathrm{e}^{i\beta}$ and substituting it into Eq. (A21), the modulation equations for the clamped-clamped SMR are obtained.

Appendix B

The coefficients in Eq. (54) for the cantilevered SMR:

$$M_{ij}=\delta_{ij}+\sum_{p=1}^{P}\beta_p\phi_i\left(\xi_P\right)\phi_j\left(\xi_P\right),\ C_{ij}=\int_0^1 c\phi_i\phi_j d\xi, \tag{B1}$$

$$\begin{aligned}K_{ij}=&\alpha_1\left(1+\mu\right)\left[\int_0^1 2\frac{\partial w_s}{\partial\xi}\frac{\partial^4 w_s}{\partial\xi^4}\frac{\partial\phi_i}{\partial\xi}\phi_j d\xi+\int_0^1\left(\frac{\partial w_s}{\partial\xi}\right)^2\frac{\partial^4\phi_i}{\partial\xi^4}\phi_j d\xi\right]\\&+\alpha_1\left(1+\mu\right)\left(\int_0^1 4\frac{\partial w_s}{\partial\xi}\frac{\partial^2 w_s}{\partial\xi^2}\frac{\partial^3\phi_i}{\partial\xi^3}\phi_j d\xi+\int_0^1 4\frac{\partial w_s}{\partial\xi}\frac{\partial^3 w_s}{\partial\xi^3}\frac{\partial^2\phi_i}{\partial\xi^2}\phi_j d\xi\right)\\&+\alpha_1\left(1+\mu\right)\left[\int_0^1 4\frac{\partial^2 w_s}{\partial\xi^2}\frac{\partial^3 w_s}{\partial\xi^3}\frac{\partial\phi_i}{\partial\xi}\phi_j d\xi+\int_0^1 3\left(\frac{\partial^2 w_s}{\partial\xi 2}\right)^2\frac{\partial^2\phi_i}{\partial\xi^2}\phi_j d\xi\right]\\&+\left(1+\mu\right)\int_0^1\frac{\partial^4\phi_i}{\partial\xi^4}\phi_j d\xi-2\alpha_2 V_{\mathrm{DC}}^2\int_0^1\frac{\phi_i\phi_j}{\left(1-w_s\right)^3}d\xi,\end{aligned} \tag{B2}$$

$$\begin{aligned}K_{ijk}=&\alpha_1\left(1+\mu\right)\left(\int_0^1\frac{\partial^4 w_s}{\partial\xi^4}\frac{\partial\phi_i}{\partial\xi}\frac{\partial\phi_k}{\partial\xi}\phi_j d\xi+\int_0^1 2\frac{\partial w_s}{\partial\xi}\frac{\partial\phi_i}{\partial\xi}\frac{\partial^4\phi_k}{\partial\xi^4}\phi_j d\xi\right)\\&+\alpha_1\left(1+\mu\right)\left(\int_0^1 4\frac{\partial w_s}{\partial\xi}\frac{\partial^2\phi_i}{\partial\xi^2}\frac{\partial^3\phi_k}{\partial\xi^3}\phi_j d\xi+\int_0^1 4\frac{\partial^2 w_s}{\partial\xi^2}\frac{\partial\phi_i}{\partial\xi}\frac{\partial^3\phi_k}{\partial\xi^3}\phi_j d\xi\right)\\&+\alpha_1\left(1+\mu\right)\left(\int_0^1 4\frac{\partial^3 w_s}{\partial\xi^3}\frac{\partial\phi_i}{\partial\xi}\frac{\partial^2\phi_k}{\partial\xi^2}\phi_j d\xi+\int_0^1 3\frac{\partial^2 w_s}{\partial\xi^2}\frac{\partial^2\phi_i}{\partial\xi^2}\frac{\partial^2\phi_k}{\partial\xi^2}\phi_j d\xi\right)\\&-3\alpha_2 V_{\mathrm{DC}}^2\int_0^1\frac{\phi_i\phi_j\phi_k}{\left(1-w_s\right)^4}d\xi,\end{aligned} \tag{B3}$$

$$\begin{aligned}K_{ijkl}=&\alpha_1\left(1+\mu\right)\left(\int_0^1\frac{\partial\phi_i}{\partial\xi}\frac{\partial\phi_k}{\partial\xi}\frac{\partial^4\phi_l}{\partial\xi^4}\phi_j d\xi+\int_0^1 4\frac{\partial\phi_i}{\partial\xi}\frac{\partial^2\phi_k}{\partial\xi^2}\frac{\partial^3\phi_l}{\partial\xi^3}\phi_j d\xi\right)\\&+\alpha_1\left(1+\mu\right)\int_0^1\frac{\partial^2\phi_i}{\partial\xi^2}\frac{\partial^2\phi_k}{\partial\xi^2}\frac{\partial^2\phi_l}{\partial\xi^2}\phi_j d\xi-4\alpha_2 V_{\mathrm{DC}}^2\int_0^1\frac{\phi_i\phi_j\phi_k\phi_l}{\left(1-w_s\right)^5}d\xi,\end{aligned} \tag{B4}$$

$$F_j=2\alpha_2 V_{\mathrm{DC}}V_{\mathrm{AC}}\int_0^1\frac{\phi_j}{\left(1-w_s\right)^2}d\xi. \tag{B5}$$

The coefficients for the doubly clamped SMR:

$$M_{ij}=\delta_{ij}+\sum_{p=1}^{P}\beta_p\varphi_i\left(x_P\right)\varphi_j\left(x_P\right),\ C_{ij}=\int_0^1 c\varphi_i\varphi_j dx, \tag{B6}$$

$$\begin{aligned}K_{ij}=&\left(1+\mu\right)\int_0^1\frac{\partial^4\varphi_i}{\partial x^4}\varphi_j dx-\left[N_F+\alpha_3\int_0^1\left(\frac{\partial w_s}{\partial x}\right)^2 dx\right]\int_0^1\frac{\partial^2\varphi_i}{\partial x^2}\varphi_j dx\\&-\alpha_3\int_0^1\left(\frac{\partial w_s}{\partial x}\right)^2\varphi_j dx\int_0^1 2\frac{\partial w_s}{\partial x}\frac{\partial\varphi_i}{\partial x}dx-2\alpha_4 V_{\mathrm{DC}}^2\int_0^1\frac{\varphi_i\varphi_j}{\left(1-w_s\right)^3}dx,\end{aligned} \tag{B7}$$

$$K_{ijk} = -2\alpha_3 \int_0^1 \frac{\partial w_s}{\partial x} \frac{\partial \varphi_i}{\partial x} dx \int_0^1 \frac{\partial^2 \varphi_k}{\partial x^2} \varphi_j dx - \alpha_3 \int_0^1 \left(\frac{\partial w_s}{\partial x} \right)^2 \varphi_j dx \int_0^1 \frac{\partial \varphi_i}{\partial x} \frac{\partial \varphi_k}{\partial x} dx$$
$$-3\alpha_4 V_{\mathrm{DC}}^2 \int_0^1 \frac{\varphi_i \varphi_j \varphi_k}{\left(1 - w_s\right)^4} dx, \tag{B8}$$

$$K_{ijkl} = -\alpha_3 \int_0^1 \frac{\partial \varphi_i}{\partial x} \frac{\partial \varphi_k}{\partial x} dx \int_0^1 \frac{\partial^2 \varphi_l}{\partial x^2} \varphi_j dx - 4\alpha_4 V_{\mathrm{DC}}^2 \int_0^1 \frac{\varphi_i \varphi_j \varphi_k \varphi_l}{\left(1 - w_s\right)^5} dx, \tag{B9}$$

$$F_j = 2\alpha_4 V_{\mathrm{DC}} V_{\mathrm{AC}} \int_0^1 \frac{\varphi_j}{\left(1 - w_s\right)^2} dx. \tag{B10}$$

References

[1] Zhang, T., Wu, J., Yang, J., Zhou, G.: A MEMS comb drive resonator with electrically tunable nonlinearity. Sens. Actuator A-Phys. **401**, 117606 (2026). https://doi.org/10.1016/j.sna.2026.117606

[2] Xu, Y., Wang, C., Ren, J., Lv, J., Shao, G., Wei, X.: Frequency stability enhancement of MEMS resonator using Duffing nonlinearity. Int. J. Mech. Sci. **313**, 111272 (2026). https://doi.org/10.1016/j.ijmecsci.2026.111272

[3] Ouakad, H.M., Alneamy, A.M.: Exploring dynamic energy transfer in electrostatically coupled micro shallow arch sensors. Chaos Solitons Fractals. **200**, 117038 (2025). https://doi.org/10.1016/j.chaos.2025.117038

[4] Peng, B.R., Zhang, X.Y., Xiao, X.Z., Li, X.F., Li, Z.: Inverse quality factor of fractional viscoelastic micro/nanobeams with surface effects based on memory-dependent heat conduction model. Int. J. Heat Mass Transfer. **252**, 127486 (2025). https://doi.org/10.1016/j.ijheatmasstransfer.2025.127486

[5] Qian, J., Wang, Y., Xue, Y., Begum, H., Fu, Y.Q., Lee, J.E.Y.: Integrated functions of microfluidics and gravimetric sensing enabled by piezoelectric driven microstructures. Appl. Phys. Rev. **12**(1), 011401 (2025). https://doi.org/10.1063/5.0225891

[6] Zhu, B., Cai, Q., Liu, Y., Zhang, S., Liu, W., He, Q., et al.: Nanometre-resolution three-dimensional tomographic and vectorial near-field imaging in dielectric optical resonators. Nat. Nanotechnol. **20**(5), 623-629 (2025). https://doi.org/10.1038/s41565-025-01873-9

[7] Wang, J., Zhang, Y.: Multi-particle mass sensing based on a single-walled carbon nanotube resonator. Appl. Math. Mech.-Engl. Ed. **47**(4), 883-904 (2026). https://doi.org/10.1007/s10483-026-3376-6

[8] Li, Y., Wang, H., Guo, Z., Zhao, X., Zhou, Y., Wang, Q., et al.: Large-scale optical trapping using a gradient-thickness protected microbottle resonator. Microsyst. Nanoeng. **12**(1), 35 (2026). https://doi.org/10.1038/s41378-026-01167-7

[9] Moser, J., Güttinger, J., Eichler, A., Esplandiu, M.J., Liu, D.E., Dykman, M.I., et al.: Ultrasensitive force detection with a nanotube mechanical resonator. Nat. Nanotechnol. **8**(7), 493-496 (2013). https://doi.org/10.1038/nnano.2013.97

[10] Zhang, X.C., Myers, E.B., Sader, J.E., Roukes, M.L.: Nanomechanical torsional resonators for frequency-shift infrared thermal sensing. Nano Lett. **13**(4), 1528-1534 (2013). https://doi.org/10.1021/nl304687p

[11] Wang, Y.X., Liang, J.G., Kim, N.Y., Zhou, X., Jiang, Y.F., Qiang, T.: Dual-band multigap resonator integrated with spiral inertial microfluidics for simultaneous label-free and high-throughput biomolecular detection. IEEE Trans. Instrum. Meas. **75**, 1-11 (2026). https://doi.org/10.1109/TIM.2026.3662841

[12] Grasta, A.l., Gómez-Gómez, M.I., Griol, A., Gómez, E., Carlo, M.D., Passaro, V.M.N., et al.: Integrated microphotonic platform for highly sensitive virus detection. Sens. Actuators Rep. **9**, 100320 (2025). https://doi.org/10.1016/j.snr.2025.100320

[13] Hanay, M.S., Kelber, S., Naik, A.K., Chi, D., Hentz, S., Bullard, E.C., et al.: Single-protein nanomechanical mass spectrometry in real time. Nat. Nanotechnol. **7**(9), 602-608 (2012). https://doi.org/10.1038/nnano.2012.119

[14] Beardslee, L.A., Addous, A.M., Heinrich, S., Josse, F., Dufour, I., Brand, O.: Thermal excitation and piezoresistive detection of cantilever in-plane resonance modes for sensing applications. J. Microelectromech. Syst. **19**(4), 1015-1017 (2010). https://doi.org/10.1109/JMEMS.2010.2052093

[15] Burg, T.P., Godin, M., Knudsen, S.M., Shen, W., Carlson, G., Foster, J.S., et al.: Weighing of biomolecules, single cells and single nanoparticles in fluid. Nature. **446**(7139), 1066-1069 (2007). https://doi.org/10.1038/nature05741

[16] Sader, J.E., Burg, T.P., Manalis, S.R.: Energy dissipation in microfluidic beam resonators. J. Fluid Mech. **650**, 215-250 (2010). https://doi.org/10.1017/S0022112009993521

[17] Zhong, Z.Y., Zhou, J.P., Zhang, H.L., Zhang, W.M., Meng, G.: Thermoelastic damping in fluid-conveying microresonators. Int. J. Heat Mass Transfer. **93**, 431-440 (2016). https://doi.org/10.1016/j.ijheatmasstransfer.2015.09.084

[18] Yan, H., Zhang, W.M., Jiang, H.M., Hu, K.M., Peng, Z.K., Meng, G.: Dynamical characteristics of fluid-conveying microbeams actuated by electrostatic force. Microfluid. Nanofluid. **20**(10), 137 (2016). https://doi.org/10.1007/s10404-016-1801-7

[19] Yan, H., Zhang, W.M., Jiang, H.M., Hu, K.M.: Pull-in effect of suspended microchannel resonator sensor subjected to electrostatic actuation. Sensors. **17**(1), 114 (2017). https://doi.org/10.3390/s17010114

[20] Dai, H.L., Wu, P., Wang, L.: Nonlinear dynamic responses of electrostatically actuated microcantilevers containing internal fluid flow. Microfluid. Nanofluid. **21**(10), 162 (2017). https://doi.org/10.1007/s10404-017-1999-z

[21] Jin, Q., Ren, Y., Yuan, F.G.: Combined resonance of pulsatile flow-transporting FG nanotubes under forced excitation with movable boundary. Nonlinear Dyn. **111**(7), 6157-6178 (2023). https://doi.org/10.1007/s11071-022-08148-1

[22] Zhao, S., Li, L., Shi, P.: Analytical solutions of functionally graded microbeam models based on the modified couple stress theory: A comparative study of Euler-Bernoulli, Timoshenko and Reddy beams. Thin-Walled Struct. **224**, 114648 (2026). https://doi.org/10.1016/j.tws.2026.114648

[23] Li, B., Zhang, C., Li, H.: The dynamic stiffness method for natural frequency calculation of curved micro-pipe conveying fluid based on modified couple stress theory. Appl. Math. Modell. **156**, 116903 (2026). https://doi.org/10.1016/j.apm.2026.116903

[24] Hu, K., Wang, Y.K., Dai, H.L., Wang, L., Qian, Q.: Nonlinear and chaotic vibrations of cantilevered micropipes conveying fluid based on modified couple stress theory. Int. J. Eng. Sci. **105**, 93-107 (2016). https://doi.org/10.1016/j.ijengsci.2016.04.014

[25] Deng, J., Liu, Y., Liu, W.: Size-dependent vibration analysis of multi-span functionally graded material micropipes conveying fluid using a hybrid method. Microfluid. Nanofluid. **21**(8), 133 (2017). https://doi.org/10.1007/s10404-017-1967-7

[26] Zhang, P., Shao, W., Arvin, H., Chen, W., Wu, W.: Nonlinear free vibrations of a nanocomposite micropipes conveying laminar flow subjected to thermal ambient: Employing invariant manifold approach. J. Fluids Struct. **135**, 104311 (2025). https://doi.org/10.1016/j.jfluidstructs.2025.104311

[27] De Pastina, A., Villanueva, L.G.: Suspended micro/nano channel resonators: a review. J. Micromech. Microeng. **30**(4), 043001 (2020). https://doi.org/10.1088/1361-6439/ab6df1

[28] Lee, J., Shen, W., Payer, K., Burg, T.P., Manalis, S.R.: Toward attogram mass measurements in solution with suspended nanochannel resonators. Nano Lett. **10**(7), 2537-2542 (2010). https://doi.org/10.1021/nl101107u

[29] Lee, J., Bryan, A.K., Manalis, S.R.: High precision particle mass sensing using microchannel resonators in the second vibration mode. Rev. Sci. Instrum. **82**(2), 023704 (2011). https://doi.org/10.1063/1.3534825

[30] Weng, Y., Delgado, F., Son, S., Burg, T., Wasserman, S., Manalis, S.: Mass sensors with mechanical traps for weighing single cells in different fluids. Lab Chip. **11**, 4174-4180 (2011). https://doi.org/10.1039/c1lc20736a

[31] Khan, M.F., Schmid, S., Larsen, P.E., Davis, Z.J., Yan, W., Stenby, E.H., et al.: Online measurement of mass density and viscosity of pL fluid samples with suspended microchannel resonator. Sens. Actuator B-Chem. **185**, 456-461 (2013). https://doi.org/10.1016/j.snb.2013.04.095

[32] Olcum, S., Cermak, N., Wasserman, S.C., Manalis, S.R.: High-speed multiple-mode mass-sensing resolves dynamic nanoscale mass distributions. Nat. Commun. **6**(1), 7070 (2015). https://doi.org/10.1038/ncomms8070

[33] Katsikis, G., Collis, J.F., Knudsen, S.M., Agache, V., Sader, J.E., Manalis, S.R.: Inertial and viscous flywheel sensing of nanoparticles. Nat. Commun. **12**(1), 5099 (2021). https://doi.org/10.1038/s41467-021-25266-3

[34] Martín-Pérez, A., Ramos, D.: Enhancing cell characterization via hydrodynamic compression in suspended microchannel resonators. Sens. Actuator A-Phys. **396**, 117161 (2025). https://doi.org/10.1016/j.sna.2025.117161

[35] Hajjaj, A.Z., Jaber, N., Ilyas, S., Alfosail, F.K., Younis, M.I.: Linear and nonlinear dynamics of micro and nano-resonators: Review of recent advances. Int. J. Non-Linear Mech. **119**, 103328 (2020). https://doi.org/10.1016/j.ijnonlinmec.2019.103328

[36] Li, L., Tang, P., Li, T., Zhang, C., Qiao, Y., Zhang, W.: Synchronous phase-switching mechanism of a 2-DOF self-excited and forced combined excitation nonlinear mechanical resonator. Mech. Syst. Signal Process. **246**, 113927 (2026). https://doi.org/10.1016/j.ymssp.2026.113927

[37] Bouchaala, A., Jaber, N., Yassine, O., Shekhah, O., Chernikova, V., Eddaoudi, M., et al.: Nonlinear-based MEMS sensors and active switches for gas detection. Sensors. **16**, 758 (2016). https://doi.org/10.3390/s16060758

[38] Nguyen, V.N., Baguet, S., Lamarque, C.H., Dufour, R.: Bifurcation-based micro-/nanoelectromechanical mass detection. Nonlinear Dyn. **79**(1), 647-662 (2015). https://doi.org/10.1007/s11071-014-1692-7

[39] Antonio, D., Zanette, D.H., López, D.: Frequency stabilization in nonlinear micromechanical oscillators. Nat. Commun. **3**(1), 806 (2012). https://doi.org/10.1038/ncomms1813

[40] Wang, J., Zhang, Y.: Mass detection based on the 3:1 internal resonance in a piezoelectric laminated microbeam resonator sensor. Nonlinear Dyn. **113**(17), 22625-22649 (2025). https://doi.org/10.1007/s11071-025-11343-5

[41] Olcum, S., Cermak, N., Wasserman, S.C., Christine, K.S., Atsumi, H., Payer, K.R., et al.: Weighing nanoparticles in solution at the attogram scale. Proc. Natl. Acad. Sci. U.S.A. **111**(4), 1310-1315 (2014). https://doi.org/10.1073/pnas.1318602111

[42] Zhang, Y., Zhuo, L.J., Zhao, H.S.: Determining the effects of surface elasticity and surface stress by measuring the shifts of resonant frequencies. P. Roy. Soc. A-Math. Phy. **469**(2159), 20130449 (2013). https://doi.org/10.1098/rspa.2013.0449

[43] Rocha, R.T., Alfosail, F., Zhao, W., Younis, M.I., Masri, S.F.: Nonparametric identification of a micro-electromechanical resonator. Mech. Syst. Signal Process. **161**, 107932 (2021). https://doi.org/10.1016/j.ymssp.2021.107932

[44] Rashidi, Z., Azizi, S., Rahmani, O.: Nonlinear dynamics of a piezoelectrically laminated initially curved microbeam resonator exposed to fringing-field electrostatic actuation. Nonlinear Dyn. **111**(22), 20715-20733 (2023). https://doi.org/10.1007/s11071-023-08915-8

[45] Zhang, Y., Liu, Y., Murphy, K.D.: Nonlinear dynamic response of beam and its application in nanomechanical resonator. Acta Mech. Sin. **28**(1), 190-200 (2012). https://doi.org/10.1007/s10409-011-0501-5

[46] Younis, M.I., Nayfeh, A.H.: A Study of the Nonlinear response of a resonant microbeam to an electric actuation. Nonlinear Dyn. **31**(1), 91-117 (2003). https://doi.org/10.1023/A:1022103118330

[47] Gaidarzhy, A., Zolfagharkhani, G., Badzey, R.L., Mohanty, P.: Evidence for quantized displacement in macroscopic nanomechanical oscillators. Phys. Rev. Lett. **94**(3), 030402 (2005). https://doi.org/10.1103/PhysRevLett.94.030402

[48] Zhang, Y.: Frequency spectra of nonlocal Timoshenko beams and an effective method of determining nonlocal effect. Int. J. Mech. Sci. **128-129**, 572-582 (2017). https://doi.org/10.1016/j.ijmecsci.2017.05.017

[49] Photiadis, D.M., Judge, J.A.: Attachment losses of high Q oscillators. Appl. Phys. Lett. **85**(3), 482-484 (2004). https://doi.org/10.1063/1.1773928

[50] Judge, J.A., Photiadis, D.M., Vignola, J.F., Houston, B.H., Jarzynski, J.: Attachment loss of micromechanical and nanomechanical resonators in the limits of thick and thin support structures. J. Appl. Phys. **101**(1), 013521 (2007). https://doi.org/10.1063/1.2401271

[51] Yan, H., Zhang, W.M., Jiang, H.M., Hu, K.M., Hong, F.J., Peng, Z.K., et al.: A measurement criterion for accurate mass detection using vibrating suspended microchannel resonators. J. Sound Vib. **403**, 1-20 (2017). https://doi.org/10.1016/j.jsv.2017.05.030

[52] Liu, D., He, Y., Tang, X., Ding, H., Hu, P., Cao, P.: Size effects in the torsion of microscale copper wires: Experiment and analysis. Scr. Mater. **66**(6), 406-409 (2012). https://doi.org/10.1016/j.scriptamat.2011.12.003

[53] Liu, D., He, Y., Dunstan, D.J., Zhang, B., Gan, Z., Hu, P., et al.: Toward a further

understanding of size effects in the torsion of thin metal wires: An experimental and theoretical assessment. Int. J. Plast. **41**, 30-52 (2013). https://doi.org/10.1016/j.ijplas.2012.08.007

[54] Abdelbaki, A.R., Païdoussis, M.P., Misra, A.K.: A nonlinear model for a hanging tubular cantilever simultaneously subjected to internal and confined external axial flows. J. Sound Vib. **449**, 349-367 (2019). https://doi.org/10.1016/j.jsv.2019.02.031

[55] Nikpourian, A., Ghazavi, M.R., Azizi, S.: On the nonlinear dynamics of a piezoelectrically tuned micro-resonator based on non-classical elasticity theories. Int. J. Mech. Mater. Des. **14**(1), 1-19 (2018). https://doi.org/10.1007/s10999-016-9357-y

[56] Nikpourian, A., Ghazavi, M.R., Azizi, S.: Size-dependent modal interactions of a piezoelectrically laminated microarch resonator with 3:1 internal resonance. Appl. Math. Mech.-Engl. Ed. **41**(10), 1517-1538 (2020). https://doi.org/10.1007/s10483-020-2658-6

[57] Wang, Z., Ren, J.: Nonlinear modal interaction of an electrically actuated microbeam with flexible support. Nonlinear Dyn. **99**(3), 1871-1891 (2020). https://doi.org/10.1007/s11071-019-05402-x

[58] Tian, Z., Xue, W., Lou, W., Liu, M., Feng, H., Wang, X., et al.: Study on anisotropic mechanical properties of single-crystal silicon at different strain rates. Micromachines. **16**(7), 744 (2025). https://doi.org/10.3390/mi16070744

[59] Dohn, S., Sandberg, R., Svendsen, W., Boisen, A.: Enhanced functionality of cantilever based mass sensors using higher modes. Appl. Phys. Lett. **86**(23), 233501 (2005). https://doi.org/10.1063/1.1948521

[60] Ghatkesar, M., Barwich, V., Braun, T., Ramseyer, J.P., Gerber, C., Hegner, M., et al.: Higher modes of vibration increase mass sensitivity in nanomechanical microcantilevers. Nanotechnology. **18**, 445502 (2007). https://doi.org/10.1088/0957-4484/18/44/445502

[61] Ardoino, N., Lunelli, L., Pucker, G., Vanzetti, L., Favaretto, R., Pasquardini, L., et al.: Optimization of surface functionalizations for ring resonator-based biosensors. Sensors. **24**(10), 3107 (2024). https://doi.org/10.3390/s24103107

[62] Lin, T., Li, S., Huang, Y., Zhong, S., Sun, F., Zhong, Y., et al.: Intense terahertz field confined metallic nanoarchitectures for targeted actively capturing and specific biosensing via multi-step surface functionalization. Sens. Actuator B-Chem. **458**, 139794 (2026). https://doi.org/10.1016/j.snb.2026.139794

[63] Mazuryk, J., Paszke, P., Pawlak, D.A., Kutner, W., Sharma, P.S.: Fabrication, characterization, and sensor applications of polymer-based whispering gallery mode microresonators. ACS Sens. **10**(8), 5314-5338 (2025). https://doi.org/10.1021/acssensors.5c00057

[64] Sypabekova, M., Kleiss, J., Hagemann, A., Schuemann, S., Wills, R., Zechmann, B., et al.: Improvement of the optical cavity-based biosensor's limit of detection using optimal 3-aminopropyltriethoxysilane process. Sci. Rep. **15**(1), 7739 (2025). https://doi.org/10.1038/s41598-025-92151-0

[65] Lee, J., Chunara, R., Shen, W., Payer, K., Babcock, K., Burg, T., et al.: Suspended Microchannel resonators with piezoresistive sensors. Lab Chip. **11**, 645-651 (2011). https://doi.org/10.1039/c0lc00447b

[66] Modena, M., Wang, Y., Riedel, D., Burg, T.: Resolution enhancement of suspended microchannel resonator for weighing of biomolecular complexes in solution. Lab Chip. **14**, (2013). https://doi.org/10.1039/c3lc51058a

[67] Folzer, E., Khan, T.A., Schmidt, R., Finkler, C., Huwyler, J., Mahler, H.C., et al.: Determination of the density of protein particles using a suspended microchannel Resonator. J. Pharm. Sci. **104**(12), 4034-4040 (2015). https://doi.org/10.1002/jps.24635

[68] Zhang, Y.: Determining the adsorption-induced surface stress and mass by measuring the shifts of resonant frequencies. Sens. Actuator A-Phys. **194**, 169-175 (2013). https://doi.org/10.1016/j.sna.2013.01.029

[69] Zhang, Y.: Detecting the stiffness and mass of biochemical adsorbates by a resonator sensor. Sens. Actuator B-Chem. **202**, 286-293 (2014). https://doi.org/10.1016/j.snb.2014.05.059

[70] Zhang, Y., Zhao, Y.P.: Mass and force sensing of an adsorbate on a beam resonator sensor. Sensors. **15** (7), 14871-14886 (2015).. https://doi.org/10.3390/s150714871

[71] Miriyala, N., Khan, M.F., Thundat, T.: Thermomechanical behavior of a bimaterial microchannel cantilever subjected to periodic IR radiation. Sens. Actuator B-Chem. **235**, 273-279 (2016). https://doi.org/10.1016/j.snb.2016.05.043

[72] Martinez, V., Behr, P., Drechsler, U., Polesel, J., Potthoff, E., Vörös, J., et al.: SU-8 hollow cantilevers for AFM cell adhesion studies. J. Micromech. Microeng. **26**, 055006 (2016). https://doi.org/10.1088/0960-1317/26/5/055006

[73] Ekinci, K.L., Yang, Y.T., Roukes, M.L.: Ultimate limits to inertial mass sensing based upon nanoelectromechanical systems. J. Appl. Phys. **95**(5), 2682-2689 (2004). https://doi.org/10.1063/1.1642738

[74] Høj, D., Wang, F., Gao, W., Hoff, U.B., Sigmund, O., Andersen, U.L.: Ultra-coherent nanomechanical resonators based on inverse design. Nat. Commun. **12**(1), 5766 (2021). https://doi.org/10.1038/s41467-021-26102-4

[75] Ko, J., Khan, F., Nam, Y., Lee, B.J., Lee, J.: Nanomechanical sensing using heater-integrated fluidic resonators. Nano Lett. **22**(19), 7768-7775 (2022). https://doi.org/10.1021/acs.nanolett.2c01572

[76] Martín-Pérez, A., Ramos, D., Gil-Santos, E., García-López, S., Yubero, M.L., Kosaka, P.M., et al.: Mechano-optical analysis of single cells with transparent microcapillary resonators. ACS Sens. **4**(12), 3325-3332 (2019). https://doi.org/10.1021/acssensors.9b02038

[77] Puumala, L., Grist, S., Newton, K., Kim, S., Kioussis, S., Chowdhury, S., et al.: Resonating with replicability: factors shaping assay yield and variability in microfluidics-integrated silicon photonic biosensors. Lab Chip. **25**, (2025). https://doi.org/10.1039/d5lc00575b

[78] Civelekoglu, O., Liu, R., Asmare, N., Arifuzzman, A.K.M., Sarioglu, A.F.: Wrap-around sensors for electrical detection of particles in microfluidic channels. Sens. Actuator B-Chem. **375**, 132874 (2023). https://doi.org/10.1016/j.snb.2022.132874

[79] Wu, W., Ishamuddin, S.H., Quinn, T.W., Yerrum, S., Zhang, Y., Debaize, L.L., et al.: High-throughput single-cell density measurements enable dynamic profiling of immune cell and drug response from patient samples. Nat. Biomed. Eng. **9**(11), 1972-1981 (2025). https://doi.org/10.1038/s41551-025-01408-6

[80] Li, L., Li, D., Yang, W., Liu, C., Dai, X., Zhang, W.: Synchronous mass detection based on 1:1:2 internal resonance of piezo-driven resonator. Int. J. Mech. Sci. **260**, 108645 (2023). https://doi.org/10.1016/j.ijmecsci.2023.108645

[81] Wang, Z., Li, M., Huang, C., Chang, J., Zhao, Z., Tan, H., et al.: Electrostatically tunable coupled double-island resonator for high-accuracy mass detection. Int. J. Mech. Sci. **319**, 111588 (2026). https://doi.org/10.1016/j.ijmecsci.2026.111588

[82] Wei, C., Zhang, Y.: Mass identification of multiple particles on a doubly clamped resonator. Sens. Actuator B-Chem. **360**, 131682 (2022). https://doi.org/10.1016/j.snb.2022.131682

[83] Dohn, S., Schmid, S., Amiot, F., Boisen, A.: Position and mass determination of multiple particles using cantilever based mass sensors. Appl. Phys. Lett. **97**(4), 044103 (2010). https://doi.org/10.1063/1.3473761

[84] Zhang, Y., Zhao, Y.P.: Mass and force sensing of an adsorbate on a string resonator. Sens. Actuator B-Chem. **221**, 305-311 (2015). https://doi.org/10.1016/j.snb.2015.06.047

[85] Stachiv, I., Machů, Z., Ševeček, O., Jeng, Y.R., Li, W.L., Kotoul, M., et al.: Achievable accuracy of resonating nanomechanical systems for mass sensing of larger analytes in GDa range. Int. J. Mech. Sci. **224**, 107353 (2022). https://doi.org/10.1016/j.ijmecsci.2022.107353

[86] Brown, S.C., Shaniv, R., Zhang, R., Reetz, C., Regal, C.A.: High-Stability mechanical frequency sensing beyond the linear regime. Nano Lett. **26**(6), 2052-2058 (2026). https://doi.org/10.1021/acs.nanolett.5c05164

[87] Xu, Y., Wang, L., Wang, C., Ren, J., Lv, J., Shao, G., et al.: Frequency stabilization in a pseudo-linear micromechanical parametric oscillator. Int. J. Mech. Sci. **280**, 109610 (2024). https://doi.org/10.1016/j.ijmecsci.2024.109610